

RL-TR-97-12
Final Technical Report
May 1997



HOLOGRAPHIC RANDOM ACCESS MEMORY

California Institute of Technology

Demetri Psaltis

APPROVED FOR PUBLIC RELEASE; DISTRIBUTION UNLIMITED.

DIGITAL QUALITY INSPECTED 4

**Rome Laboratory
Air Force Materiel Command
Rome, New York**

19970929 019

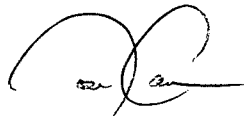
This report has been reviewed by the Rome Laboratory Public Affairs Office (PA) and is releasable to the National Technical Information Service (NTIS). At NTIS it will be releasable to the general public, including foreign nations.

RL-TR-97-12 has been reviewed and is approved for publication.



APPROVED:

ALBERT A. JAMBERDINO
Project Engineer



FOR THE COMMANDER:

JOSEPH CAMERA, Technical Director
Intelligence & Reconnaissance Directorate

If your address has changed or if you wish to be removed from the Rome Laboratory mailing list, or if the addressee is no longer employed by your organization, please notify RL/IRAP, 32 Hangar Road, Rome, NY 13441-4114. This will assist us in maintaining a current mailing list.

Do not return copies of this report unless contractual obligations or notices on a specific document require that it be returned.

REPORT DOCUMENTATION PAGE			Form Approved OMB No. 0704-0188
<p>Public reporting burden for this collection of information is estimated to average 1 hour per response, including the time for reviewing instructions, searching existing data sources, gathering and maintaining the data needed, and completing and reviewing the collection of information. Send comments regarding this burden estimate or any other aspect of this collection of information, including suggestions for reducing this burden, to Washington Headquarters Services, Directorate for Information Operations and Reports, 1215 Jefferson Davis Highway, Suite 1204, Arlington, VA 22202-4302, and to the Office of Management and Budget, Paperwork Reduction Project (0704-0188), Washington, DC 20503.</p>			
1. AGENCY USE ONLY (Leave blank)	2. REPORT DATE	3. REPORT TYPE AND DATES COVERED	
	May 1997	Final	Jun 94 - Jun 96
4. TITLE AND SUBTITLE		5. FUNDING NUMBERS	
HOLOGRAPHIC RANDOM ACCESS MEMORY		C - F30602-94-C-0182 PE - 62702F PR - 4594 TA - 15 WU - L2	
6. AUTHOR(S)		8. PERFORMING ORGANIZATION REPORT NUMBER	
Demetri Psaltis		N/A	
7. PERFORMING ORGANIZATION NAME(S) AND ADDRESS(ES)		10. SPONSORING/MONITORING AGENCY REPORT NUMBER	
California Institute of Technology 1200 California Avenue, Mail Stop 136-93 Pasadena, CA 91125		RL-TR-97-12	
9. SPONSORING/MONITORING AGENCY NAME(S) AND ADDRESS(ES)		11. SUPPLEMENTARY NOTES	
Rome Laboratory/IRAP 32 Hangar Road Rome, NY 13441-4114		Rome Laboratory Project Engineer: Albert Jamberdino/IRAP/(315) 330-4581	
12a. DISTRIBUTION AVAILABILITY STATEMENT		12b. DISTRIBUTION CODE	
Approved for public release; distribution unlimited.			
13. ABSTRACT (Maximum 200 words) We designed and demonstrated a fully working, large-scale random-access holographic memory. The recording medium is a Fe-doped LiNbO ₃ photorefractive crystal. The storage capacity of the memory is limited by the dynamic range and geometric limitation. The number of holograms stored at a certain location in the crystal is mainly limited by the dynamic range. To further increase the storage capacity, holograms can be stored at different spatial locations in the crystal. The total number of storage locations is restricted by the geometric limitations of the optical system. Three multiplexing techniques -- angle, fractal and spatial multiplexing are employed to superimpose multiple holograms in the recording medium with the help of a custom-designed segmented mirror array. The memory consists of 16 vertically spaced locations on the recording medium, a LiNbO ₃ crystal, each containing 10,000 holograms. The data storage on each of the 16 locations is organized as 4 fractal multiplexed rows of 2,500 angularly-multiplexed holograms. We successfully demonstrated the storage of 160,000 holograms in the system by recording 10,000 holograms on each of the top, center, and bottom storage locations and 1,000 holograms on each of the 16 locations. We achieved an average bit-error probability on the order of 10 ⁻⁴ . By using an acousto-optic deflector (AOD) as the angle scanner, we achieved a random access time in the order of 100 microseconds to the 1,000 holograms stored by angle multiplexing. In the latest progress towards a practical non-volatile memory system, we recorded and thermally fixed 1,000 holograms with no degradation in the error performance.			
14. SUBJECT TERMS		15. NUMBER OF PAGES	
Optical Memories, Holographic Storage, Random Access Memory, Fractal Multiplexing, Mirror Array		80	
17. SECURITY CLASSIFICATION OF REPORT		18. SECURITY CLASSIFICATION OF THIS PAGE	
UNCLASSIFIED		UNCLASSIFIED	
19. SECURITY CLASSIFICATION OF ABSTRACT		20. LIMITATION OF ABSTRACT	
UNCLASSIFIED		UL	

CONTENTS

1.	Introduction.....	1
2.	Holographic Random Access Memory Design	4
3.	Holographic Random Access Experiment	23

1 INTRODUCTION

In volume holographic memories data is stored as interference patterns formed by coherent beams of light. The 2D page-formatted information is imprinted on the object beam by a Spatial Light Modulator (SLM). Multiple pages of data are superimposed within the same volume of a storage medium. These pages, stored as separate holograms, can be independently accessed by changing either the angle, wavelength or phase code of the reference (non-information-bearing) beam. Other techniques, such as peristrophic, shift multiplexing have been proposed and demonstrated.

The nature of this page-formatted memory make it possible for both the high readout rates thanks to the parallel(2D) access and large storage capacity. Assuming one bit per pixel, current spatial light modulator (SLM) technology can provide 10^5 — 10^6 bits per stored page. If the random-access time for a page of data is $100\mu\text{sec}$. which is achievable with a non-mechanical addressing device, the readout rate is 1—10 Gbits/s. The storage capacity C can be written as $C = N_p M$, where N_p is the number of bits in each stored page, and M is the number of pages superimposed in the same volume. This will give us a capacity of 1—10 Gbits with 10,000 holograms. In addition, spatial multiplexing can be used to increase the storage capacity by recording in different spatial locations in the recording medium. Given N_l as the number of storage locations, the capacity $C = N_p M N_l$ is increased by a factor of N_l .

1.1 Dynamic range and $M/\#$

Photorefractive crystals are widely used for holographic storage because incident light modulates their index of refraction. Unfortunately, the same effect tends to erase already stored holograms during exposure of subsequent gratings. It means that the storage of multiple holograms involves both recording and erasure behavior. Therefore, the dynamic range of a photorefractive holographic storage system is different from the material dynamic range of the photorefractive crystal in which the subsequent recording erases the previously stored holograms and in effect releases part of the dynamic range used up by the previously recorded holograms.

Because of the erasure during the recording, special recording schedule is required for storing multiple holograms of equal diffraction efficiency. For instance, the recording schedule is a carefully chosen set of decreasing expo-

sure times. Initial holograms start with a large diffraction efficiency, and are erased by the exact amount needed to match the diffraction efficiency of the final short exposure.

To calculate the proper set of exposure times, each hologram is assumed to evolve during recording as

$$A_0(1 - e^{-t/\tau_r}) \approx \left(\frac{A_0}{\tau_r}\right) t \quad (1)$$

and decay during erasure as e^{-t/τ_e} . A_0 is the saturation strength of the hologram, τ_r is the characteristic recording time constant, and τ_e the characteristic erasure time. Using a simple “backwards” recursion algorithm, the set of exposure times t_1, t_2, \dots, t_{M-1} could be calculated from the last exposure time t_M , where M is the number of holograms. For a large number of holograms M , the final equalized diffraction efficiency is

$$\eta = \left[\left(\frac{A_0}{\tau_r} \right) \frac{\tau_e}{M} \right]^2 = \left[\left(\frac{A_0}{\tau_r} \right) t_M \right]^2 \quad (2)$$

We define $M/\#$ as

$$M/\# = \left(\frac{A_0}{\tau_r} \right) \tau_e, \quad (3)$$

so that

$$\eta = \left[\frac{M/\#}{M} \right]^2. \quad (4)$$

The $M/\#$ is the constant of proportionality between diffraction efficiency and the number of holograms squared. It is a measure of the consumption of the material dynamic range by the holograms.

1.2 Multiplexing techniques

The most common technique to store multiple holograms in a thick recording medium is angle multiplexing. In angle multiplexing, we use a discrete set of reference plane waves which vary in illumination angle. The wave vectors for all of these beams lie in a single plane which includes the central signal wave vector. The diffraction efficiency of a hologram is a strong function of angular change of the reference beam in this plane. Since this angle “selects” the hologram, we refer to this as the selectivity function. When the readout beam is identical to the wavefront used for recording, we are at a central peak

in the selectivity function and are “Bragg-matched”. The angular spacing between the central peak and the first null is referred to as the angular or Bragg selectivity, and can be written as

$$\Delta\theta = \frac{\lambda}{L} \frac{\cos\theta_S}{\sin(\theta_R + \theta_S)}, \quad (5)$$

where θ_S and θ_R are the incidence angles of the object and reference beams, and L is the thickness of the volume.

The 90°-geometry, where the object and reference beam enter the photorefractive crystal through orthogonal faces, has the strongest angular selectivity which is λ/L , thus allowing optimal use of the angular scanning range of the reference beam. In addition, in the 90°-geometry, the interaction length can be increased simply by extending the length of the crystal, increasing diffraction efficiency as well as Bragg selectivity. Other merits include reduced Fresnel loss, and scattered noise which tend to cluster along the direction of the reference beam.

Besides the dynamic-range limitation represented by the $M/\#$, there are geometric limitations, namely the Space-Bandwidth Product (SBP) of the optical system, especially the reference arm. To store 10,000 holograms by angle multiplexing, the reference arm needs to provide 10,000 distinct angles, in other words, the SBP of the reference arm should be at least 10,000. This requires that the SBP of both the lens system and the angle-scanning device in the arm be at least 10,000. This is sometimes very hard to satisfy. For example, the Acousto-Optic Device (AOD), one of the non-mechanical angle addressing devices commercially available, provides SBP only on the order of 1,000 or so. And even if the numeric aperture of the optical system is good enough to support a SBP of 10,000, for those angles which use the edge of the lenses, the severe aberration will deteriorate the quality of the plane-wave reference beam thus make the angle selectivity worse.

It is important to note that the Space-Bandwidth Product requirement is one dimensional because angle multiplexing is one dimensional. In order to alleviate the 1-D SBP overloading, we can take advantage of the 2-D nature of optics, and spread out the SBP loading in another dimension by using another multiplexing technique—fractal multiplexing.

We have mentioned that the angle-multiplexed reference beam angles used for separate holograms must be distinct, and that the distinction is usually created by angle changes in the plane of interaction of the reference and object beams due to Bragg selectivity. Angle changes orthogonal to this plane

of interaction have little effect on the phase-buildup of the reconstructed hologram. So unlike in angle multiplexing, reference beams which are deflected vertically can still readout the hologram. However, the reconstructed hologram is not directed along the signal axis, but tilted vertically by the same vertical angle deflection of the reference beam. In practice, the vertical bandwidth of the signal is limited. Therefore, if the vertical deflection of the reconstruction is greater than the vertical bandwidth of the signal, no signal will be detected by the detector array centered on the signal axis. Thus, we can record another new hologram at this vertical angle with no crosstalk from the others. This is called fractal multiplexing, or out-of-plane multiplexing.

Angle and fractal multiplexing are the techniques to superimpose multiple holograms in the same spatial location—same volume in the crystal. The total number of holograms we can record by angle and fractal multiplexing is determined by the dynamic range, namely, the $M/\#$. In order to further increase the storage capacity, spatial multiplexing is used to store holograms at different locations on the crystal. Spatial multiplexing is not limited by the dynamic range but by the size of the signal transverse dimension, the recording medium and the geometric limitations of the signal arm.

2 Holographic Random-Access Memory: Design

2.1 Mirror Array

Theory of operation The motivation behind the mirror array is the desire to use one angle deflector for angle multiplexing, and a co-located and orthogonal angle deflector for spatial multiplexing. The best place to start explaining how it works is the standard angle-multiplexing reference arm shown in Figure 1(a). The deflection created by an angle scanner is imaged to the surface of the crystal with a 4-F system. An angle change of the reference beam at the scanner becomes a position change in the center of the 4-F system. Likewise, an angle change in this center plane becomes a position change at the surface of the crystal. However, technically, it is very difficult to put an angle deflector in this plane without seriously limiting the deflection range of the first deflector.

To see how the mirror array solves this dilemma, we note that we can place a fixed mirror in the center focal plane without affecting the operation

of the 4-F system (Figure 1(b)). The reference beam is a focused spot at the surface of the mirror. To angle-multiplex holograms with the reference beam, the focused spot traces a horizontal path across the surface of the fixed mirror. If we were to remove all of the mirror surface above and below this horizontal path, leaving only a thin mirror strip, the operation of the system would be unchanged. We can then place additional mirror strips in this newly vacated region, and orient each with its own fixed deflection angle. The result is a vertically stacked array of long thin mirror strips which we use to create our desired angle change in the center plane.

Figures 2(a) and (b) diagram the operation of such a mirror array—Figure 2(a) shows selection of output location by the vertical angle scanner (AOD), while Figure 2(b) shows angle multiplexing at a spot by the horizontal AOD. The deflection angle of the vertical AOD determines which mirror strip will be illuminated. Each mirror strip is tilted in both dimensions in order to redirect incident light to one of the storage locations in the crystal. The horizontal angle of incidence is determined by the horizontal position of the focused spot on the mirror strip (Figure 2(b)). In this way, the 2-D angle scanner selects the position and incidence angle of the reference beam at the crystal surface. In an actual system, we need to use a beamsplitter so that the surface of the mirror array can be exactly in the center focal plane. This allows us to minimize the vertical size of each mirror strip, yet still avoid crosstalk to other storage locations. Note also that the same mirror array can be used to combine spatial multiplexing with either wavelength or phase-code multiplexing.

Since current AOD technology provides SBP on the order of 1000 or so, storage of up to 10,000 angle-multiplexed holograms at each location might be problematic. The horizontal AOD is overloaded by the large number of angles required, while the vertical AOD is underutilized. The SBP requirement also affects the size of the lens apertures needed in the reference arm. This is graphically shown in Figure 3(a), where we show the SBP load by indicating the portion of the lens aperture which is used. One solution for this asymmetric SBP loading is to use multiple mirror facets for each location. This reduces the number of angularly multiplexed holograms required per facet, dividing the SBP load evenly between the horizontal and vertical deflectors (Figure 3(b)). In using multiple mirror facets for a location, we are performing fractal multiplexing.

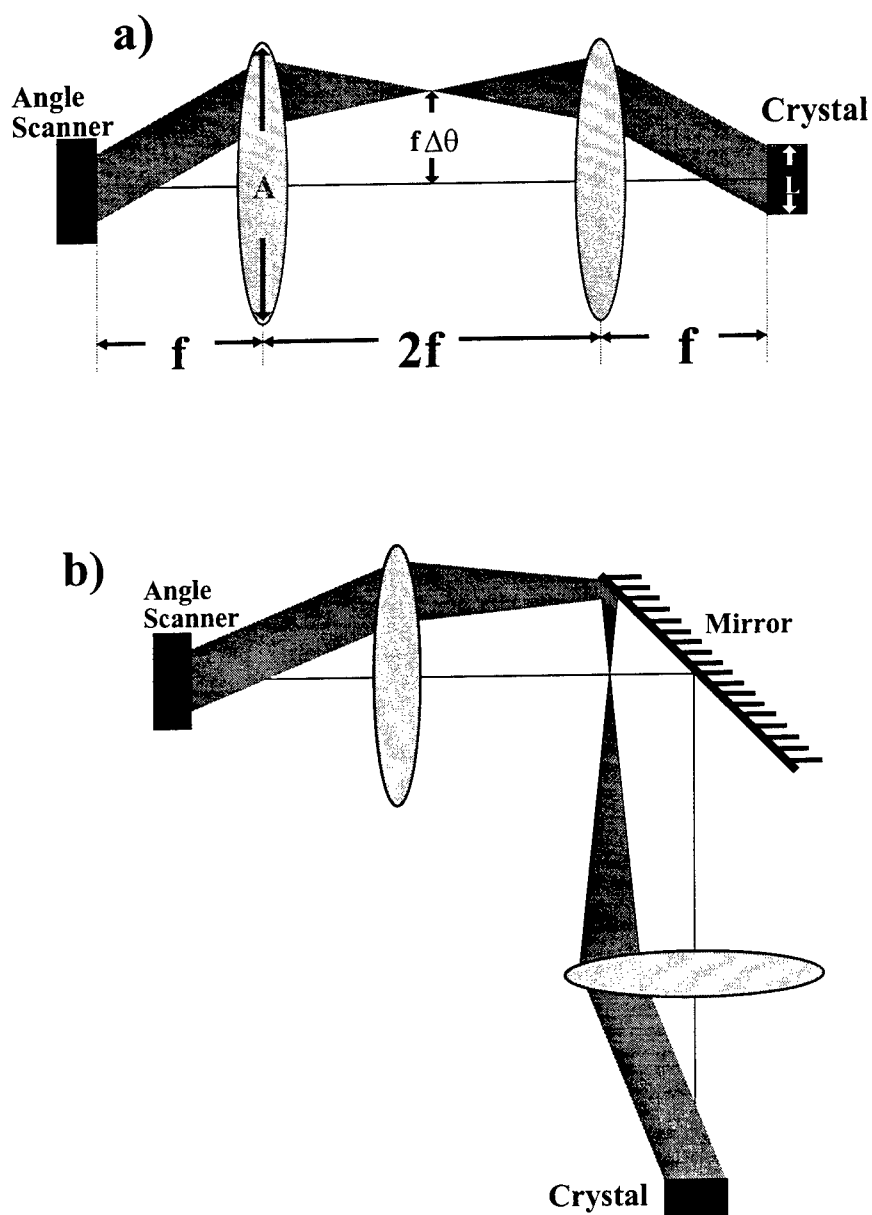


Figure 1: Angle-multiplexed holographic memory using an angle scanner.

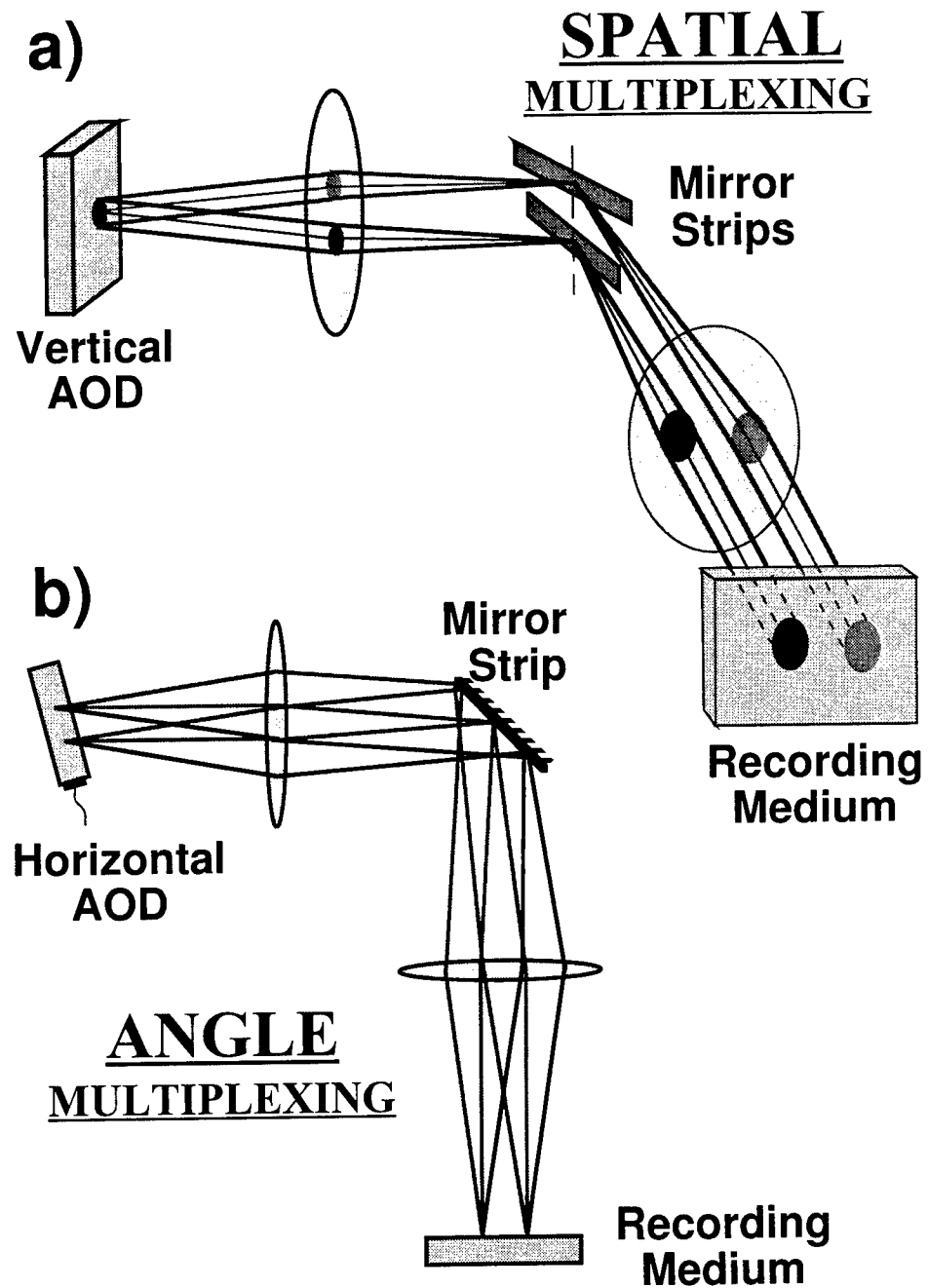


Figure 2: Operation of mirror array segments. (a) Selection of spatial location by vertical beam deflection. (b) Selection of incident reference beam angle by horizontal beam deflection.

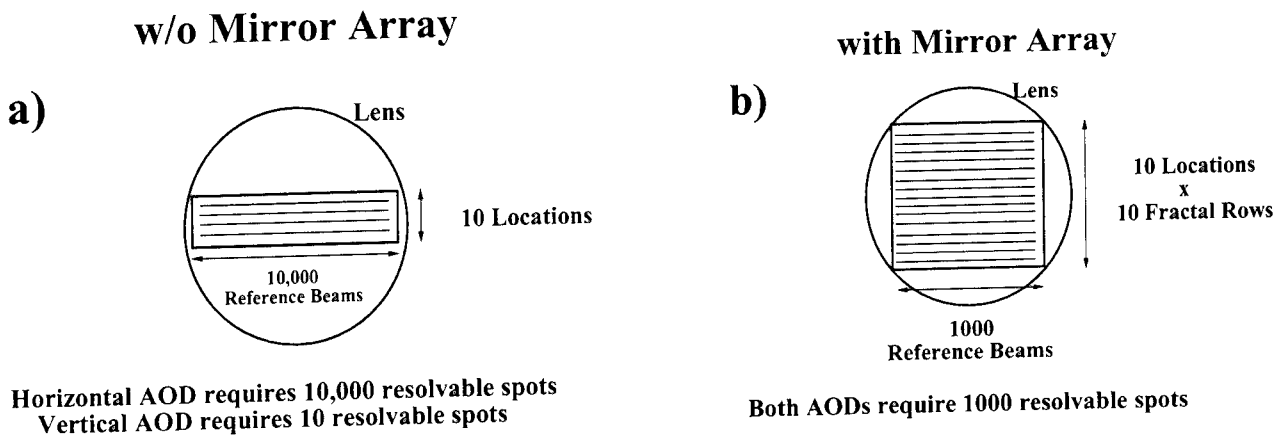


Figure 3: Space-bandwidth loading without and with mirror array

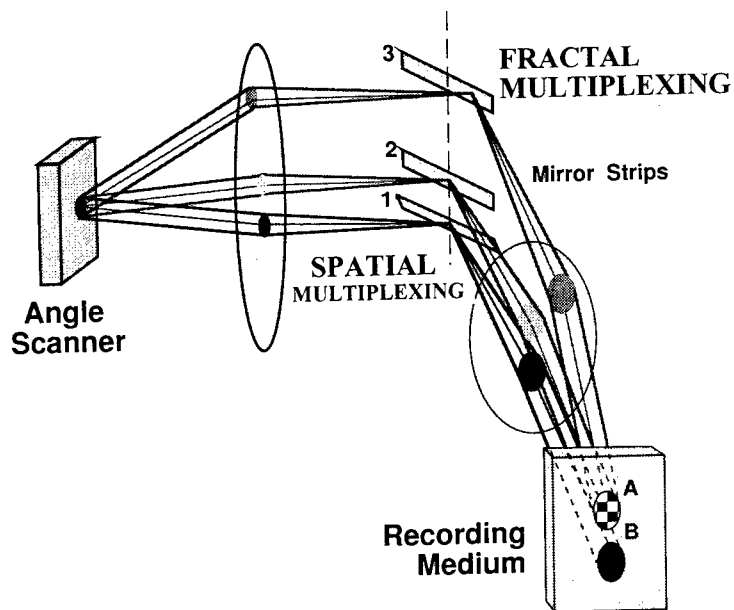


Figure 4: Implementation of fractal multiplexing with the mirror array.

MIRROR ARRAY SCHEMATIC

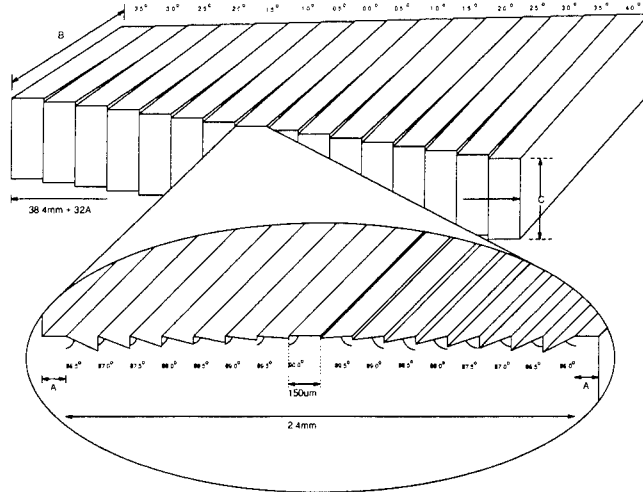


Figure 5: Mirror Array schematic.

First-generation device Figure 4 shows how fractal multiplexing works in the context of the mirror array. Mirror strips 1 and 2 perform the expected spatial multiplexing at locations A and B . Mirror strip 3 is oriented parallel to strip 2, but displaced vertically. Beams deflected to strip 3 also arrive at storage location A , but with a different vertical incidence angle than those arriving via strip 2. If the vertical separation between strips 2 and 3 is larger than the vertical bandwidth of the images being stored, then each can be used to store and retrieve holograms independently.

The schematic of the mirror array is shown in Figure 5. There are 256 mirror strips—one for each location on the crystal. Each mirror strip is $150\mu\text{m}$ wide and 75mm long. The mirror array is composed of 16 “tiles,” each of which has 16 mirror strips cut as grooves. The change in angle between tiles and between groove faces is 0.5° . The angular change between tiles is orthogonal to the increment between grooves, allowing tilting of individual facets in both directions. This mirror array was designed for spatial multiplexing over a 2-D grid of 16×16 locations. We can use the same mirror array for fractal multiplexing at each of 16 locations by removing the tilt between the tiles. Each tile contains a set of 16 vertical tilts for 16 locations—and each location has 16 mirror strips “pointed” at it, one from each tile. The separation between identically tilted mirror strips is $16 \times$ the strip width, or 2.4mm .

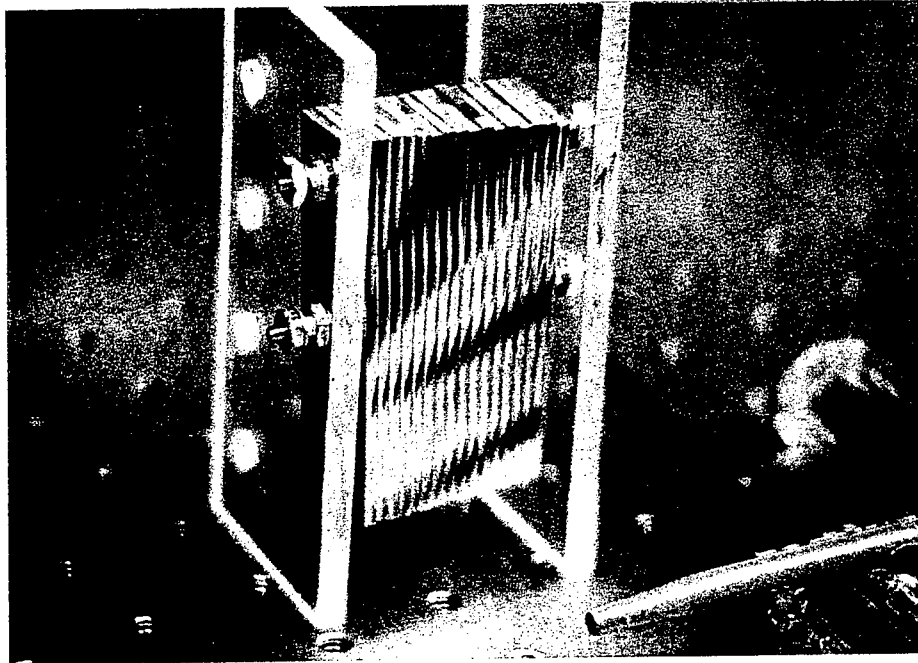


Figure 6: Mirror Array: Photograph

A prototype mirror array was fabricated with standard blazed grating technology. This technique involves cutting grooves with a diamond tip in a gold surface on a brass substrate. The groove angles are controlled by the tilt of the tip with respect to the substrate, while the groove width is set by the dimensions of the tip. An error in programming the diamond tip angles during fabrication of our prototype caused the actual change in angle between mirror strips to be 1° . The mirror array (each containing 16 mirror strips) is held together by two rods which pass through the tiles. Two holes were drilled on each tile for these rods—one in the same “reference” position, and one at a different offset on each tile. As a result, the rods hold the mirror strips like a fan with an angle change between each tile of 0.5° . We could make all the tiles parallel by pulling the second rod out and retightening the first—this is what we did to enable the fractal multiplexing over a 1-D grid. We show a photograph of the finished mirror array (aligned for the 2-D grid) in Figure 6.

2.2 Memory Design

160,000 hologram system We describe a page-formatted random-access holographic memory designed to store 160,000 holograms. The segmented

mirror array allows rapid access to any of the stored holograms with a non-mechanical angle scanner. The memory consists of 16 vertically spaced locations, each containing 10,000 holograms. Each location is organized as 10 fractal–multiplexed rows of 1000 angularly–multiplexed holograms each. This assignment requires a horizontal SBP of 1000 and a vertical SBP of 160, comfortably within the capabilities of currently available AODs. The total storage capacity is 160 Gbits¹ and a random access time determined by the 2-D angle scanner. If this is a pair of crossed AODs, the access time can be less than 100 μ sec.

The system design is shown in Figure 7. A laser beam is split in two parts and then brought together at a storage location within a stack of photorefractive crystals. The object beam is imprinted with the information displayed upon the input SLM, while the reference beam is a plane wave. A segmented mirror array and two crossed acousto-optic deflectors (AODs) allow the reference arm of the system to control both the position and angle of incidence of the reference beam. Another AOD is used to deflect the object beam to control the position of the information-bearing object beam on the crystals. The Doppler shift introduced by the AODs is compensated in the object arm by an electro-optic modulator (EOM), so that the interference pattern is stationary during storage.

We demonstrate the various elements of this design in the next section. This includes

- storage using the mirror array,
- storage of 1000 holograms using an AOD,
- storage of 10,000 holograms at a single location,
- storage at each of the 16 locations using the mirror array, and
- demonstration of 10,000 holograms at the top, center, and bottom locations.

In most of our experimental demonstrations, we use a mechanical scanner to deflect the focused spot over the surface of the mirror array.

In the remainder of this section, we discuss the lens design issues involved with bringing the signal and reference beams to the crystal, and the

¹assuming 1000 \times 1000 pixels in the SLM.

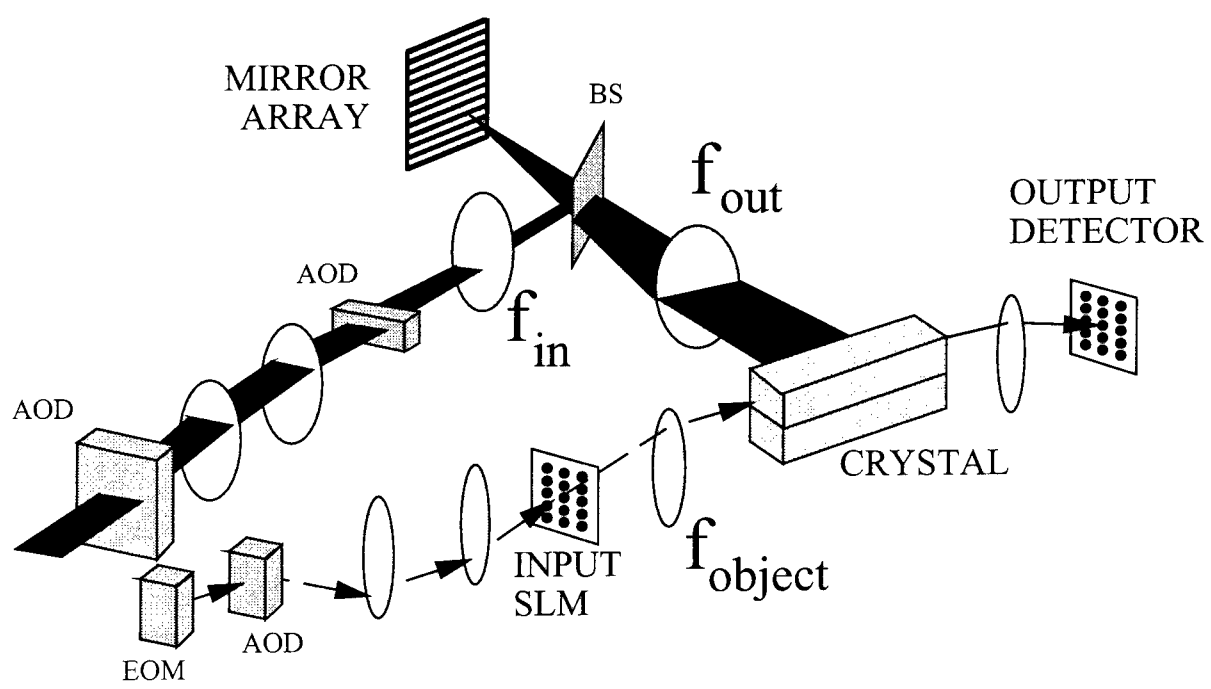


Figure 7: 160,000 hologram system

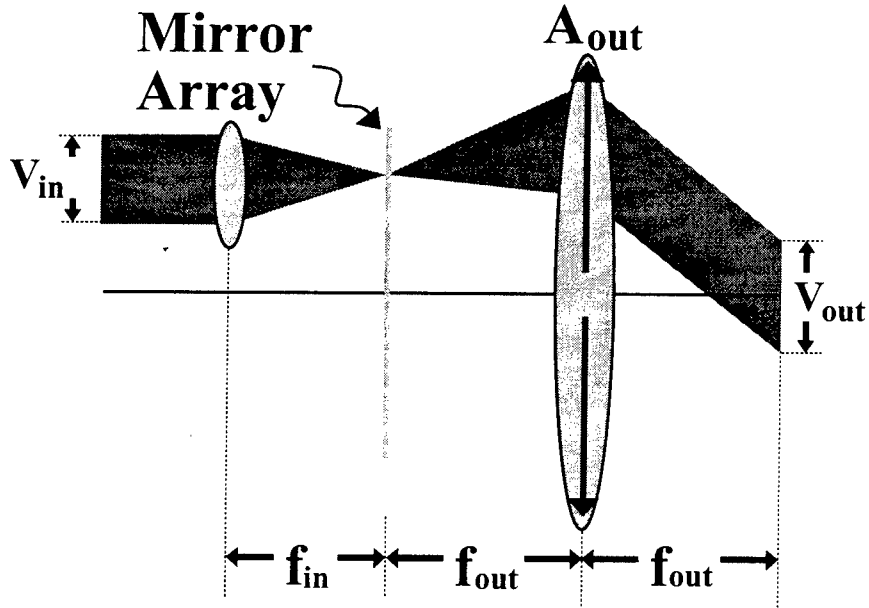


Figure 8: Reference beam with mirror array

reconstructed holograms to the detector array. We concentrate on the lens constraints involved with a mechanically accessed setup. We describe the design we have built in our laboratory, using the first-generation mirror array and commercially available lenses and discuss some of the drawbacks of this design.

Lens constraints We start our analysis with the reference beam. As shown in Figure 8, a focused spot illuminates the mirror array surface and is then directed through a lens to the crystal. Between the mirror array and the output lens, the beam passes through a circular quarter-wave plate and cube beamsplitter (not shown for simplicity). Figure 8 introduces several variables to describe the beam, the apertures, and the mirror array. These include

A_{out}	Aperture of the output lens
f_{in}, f_{out}	Focal lengths of the two lenses
V_{in}, V_{out}	Vertical dimension of the plane wave
H_{in}, H_{out}	Horizontal dimension of the plane wave
d_{facet}	Mirror strip width (150 μm in our device)
$\Delta\theta$	Vertical angle change between neighboring mirror strips (1° in our device)

Note that since we are scanning the input lens mechanically in the laboratory, we do not need to worry about its aperture.

We will first deal with the spatial and fractal multiplexing, and then see how the apertures of the output lens, beamsplitter, and waveplate affect the system. The output beam dimensions are set by the choice of focal lengths and the input beam dimensions as follows:

$$\begin{aligned} H_{out} &= \frac{f_{out}}{f_{in}} H_{in} \\ V_{out} &= \frac{f_{out}}{f_{in}} V_{in}. \end{aligned} \quad (6)$$

The input beam height V_{in} can not be too small, or the focused spot will be larger than the mirror strip width. This constraint can be written as

$$d_{facet} > \frac{\lambda}{f_{in}} V_{in}. \quad (7)$$

The vertical spacing between storage locations must be larger than the beam dimension in order to keep the storage locations distinct, as shown in Figure 9. This calls for

$$V_{out} < 2\Delta\theta f_{out}. \quad (8)$$

Now we need to deal with the interaction between the signal beam and the reference beam. The vertical extent of the stack of 16 locations is given by 16 × the right side of Equation 8. The signal arm must be able to deliver the information-bearing beam to the crystal locations within this stack, and then return the reconstructions to the same on-axis array detector, all without noticeable distortion. We could write an expression here for the aperture of the object beam lens, f_{object} , but it turns out the off-axis imaging performance of this lens is a more stringent requirement. We will discuss in the next section.

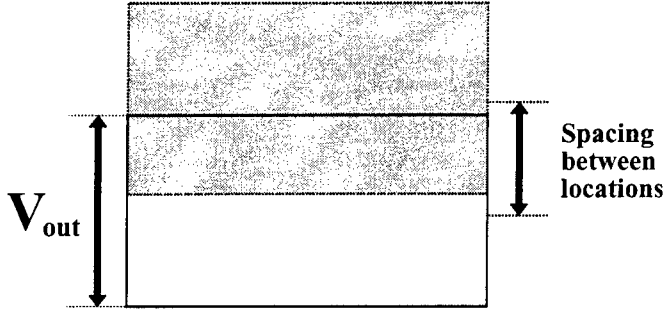


Figure 9: Isolation of spatially multiplexed locations

We need to keep the reconstructions from the various fractal rows from overlapping at the detector array. In order to use two identically tilted mirror strips to store holograms, their vertical separation (expressed in terms of angle at the crystal surface) must be larger than the vertical bandwidth of the image. We can write this as

$$\frac{m \times SLMheight}{f_{object}} < n \frac{16 \times d_{facet}}{f_{out}}, \quad (9)$$

where f_{object} the focal length of the Fourier transform lens in the object beam, m is the magnification in the object beam, and n is the number of mirror tiles between mirror strips used for fractal multiplexing. As shown in Figure 10, when Equation 9 is not satisfied then multiple output images (from different fractal rows) overlap at the array detector.

The final consideration on the signal beam is that the height of the reference beam overlaps the Fourier transform of the information-bearing beam. If this condition is not met, then the hologram will be an incomplete copy of the signal beam. If the crystal is at the exact Fourier transform plane and there is incomplete overlap, then the output will be spatially filtered; if the crystal is not in this plane, portions of the SLM image may be missing. The object beam requirement can be written as

$$V_{out} > \frac{\lambda f_{object}}{\delta} = \frac{\lambda f_{object}(\# of SLM pixels)}{m(SLMheight)}, \quad (10)$$

where we have used the relationship between the number of SLM pixels, the SLM size at the image plane of lens f_{object} , and δ . Note that Equation 10 would imply that f_{object} ought to be small, but Equation 9 indicates that

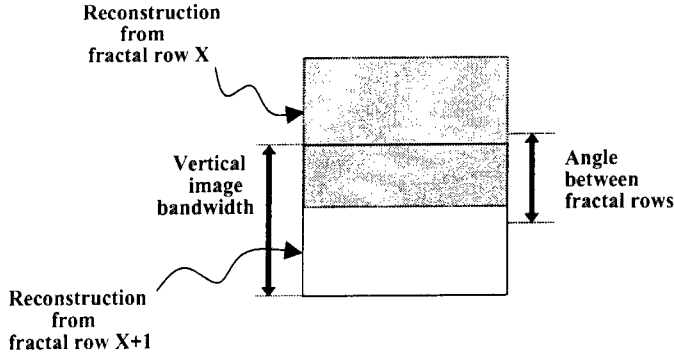


Figure 10: Separation of images from different fractal rows

f_{object} should be large. There is a tradeoff between the number of fractal rows and the vertical bandwidth of the signal beam. This is equivalent to saying that the total vertical bandwidth of the object beam is fixed—no matter how you decide to divide it into SLM pixels and fractal rows, the product of the number of pixels and the number of fractal rows is unchanged.

Aperture limitations between the mirror array and the crystal can be caused by the output lens, the cube beamsplitter, or the quarter-wave plate (Figure 11). If the apertures are too small vertically, then the beam leaving a particular mirror strip does not make it to the crystal. Too small horizontally, and the angular multiplexing range is limited. In general, the two effects are coupled, and we begin to lose angular multiplexing range towards the top and bottom of the mirror array.

When determining if the beam will pass the aperture, there are three reasons that the reference beam might approach the edge of an aperture. The first is the initial position of the focused point on the mirror strip. Vertically this is the mirror strip position, horizontally the multiplexing angle. The second contribution is the angular deflection caused by the mirror array, and the third is the non-zero size of the output beam at the aperture. We can write these as

$$Vertical\ half-aperture > y_{focus} + 2d \tan(k \delta\theta) + V_{out} \frac{d}{f_{out}} \quad (11)$$

$$Horizontal\ half-aperture > x_{focus} + 0 + H_{out} \frac{d}{f_{out}}, \quad (12)$$

where d is the distance of the aperture from the mirror array, x_{focus} & y_{focus} give the position of the focused spot on the mirror array, and $k\delta\theta$ is the deflec-

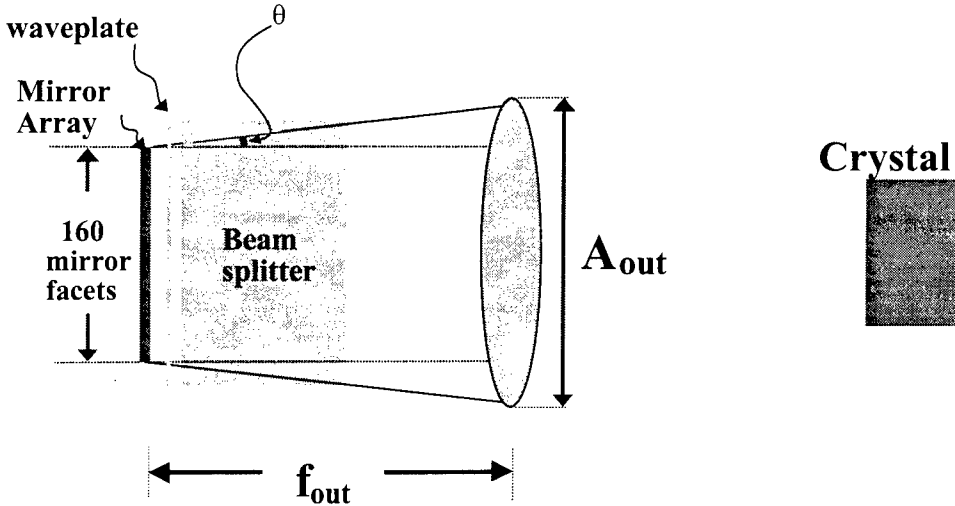


Figure 11: Apertures between the mirror array and the crystal

tion angle of the mirror strip being illuminated ($k = -8, -7, \dots, 6, 7$). We can use these equations to map out which mirror strips are usable, and how much horizontal movement we can make on each mirror strip. We can express the result in terms of angle-multiplexing “zeroes.” Note that Equations 11 and 12 are probably more restrictive than they could be. We consider only the range of horizontal angles for which the entire width of the reference beam passes the aperture. However, we can still use reference beams which are partially occluded by the apertures. Since the interaction length is smaller, we will need to space holograms farther apart (in angle) at these large reference beam angles. But we should be able to get more angle-multiplexed holograms per mirror strip, if this should be necessary.

In the case of a circular aperture such as a waveplate or lens, the vertical aperture and horizontal aperture are not independent. The horizontal aperture of such an aperture will be a function of the y position at which the beam strikes, as

$$\text{Horizontal half-aperture} = \sqrt{\text{Radius}^2 - y^2}, \quad (13)$$

where the value of y is given by the right-hand side of Equation 11. Now we are in good shape: we know where the apertures are (d) and how big they are. Given a mirror strip (y_{focus} and k), we can determine whether it can direct reference beams to the crystal, and how much angle multiplexing range we will have with it. We will discuss this in the next section.

Variable	Design #1	Design #2
H_{out}	2cm	2cm
# SLM pixels, vertical	440	440
height of SLM	2cm	2cm
f_{out}	12cm	7cm
A_{out}	10cm	7cm
vertical spacing between each location	.42cm	.24cm
total vertical extent of the 16 locations	6.7cm	3.9cm
SLM magnification	0.333	0.67
f_{object}	30cm	20cm
A_{object}	8.2cm	7cm
vertical extent of the object beam Fourier transform	0.97cm	0.32cm

Table 1: Design variables for 160,000 hologram system

2.3 Design of the mechanically accessed system

Our approach to designing a lens system is to pick a set of off-the-shelf lenses which satisfy Equations 6–10. Since we are mostly interested in demonstrating storage of holograms, we are willing to sacrifice a little on Equation 10 and lose some vertical spatial frequencies from our image. If we need, we can reallocate the pixels lost in this dimension to the horizontal dimension, since we have a lot of tolerance in this direction. We then check our design to see if the object beam deflected to the top and bottom locations can be returned to the on-axis CCD detector without distortion. Because this requires precise knowledge of the aberration performance of the particular lenses to be used, we perform this step empirically. Then, once we have a set of lenses which allow access to 16 locations, we determine how many reference beam angles we have at each location.

We show the parameters of our first design in the center column of Table 1. The first few lines show variables which were constrained by other parts of the holographic system. These include our desire to use a 2cm wide crystal, the dimensions of the Epson 480 × 440 SLM, and the parameters of the prototype mirror array. Equation 5 and 7 give the required dimensions of the beam which is input to lens f_{in} , and Equation 6 is readily satisfied by reference beams which are larger than 0.5mm or so. Equation 7 gives the

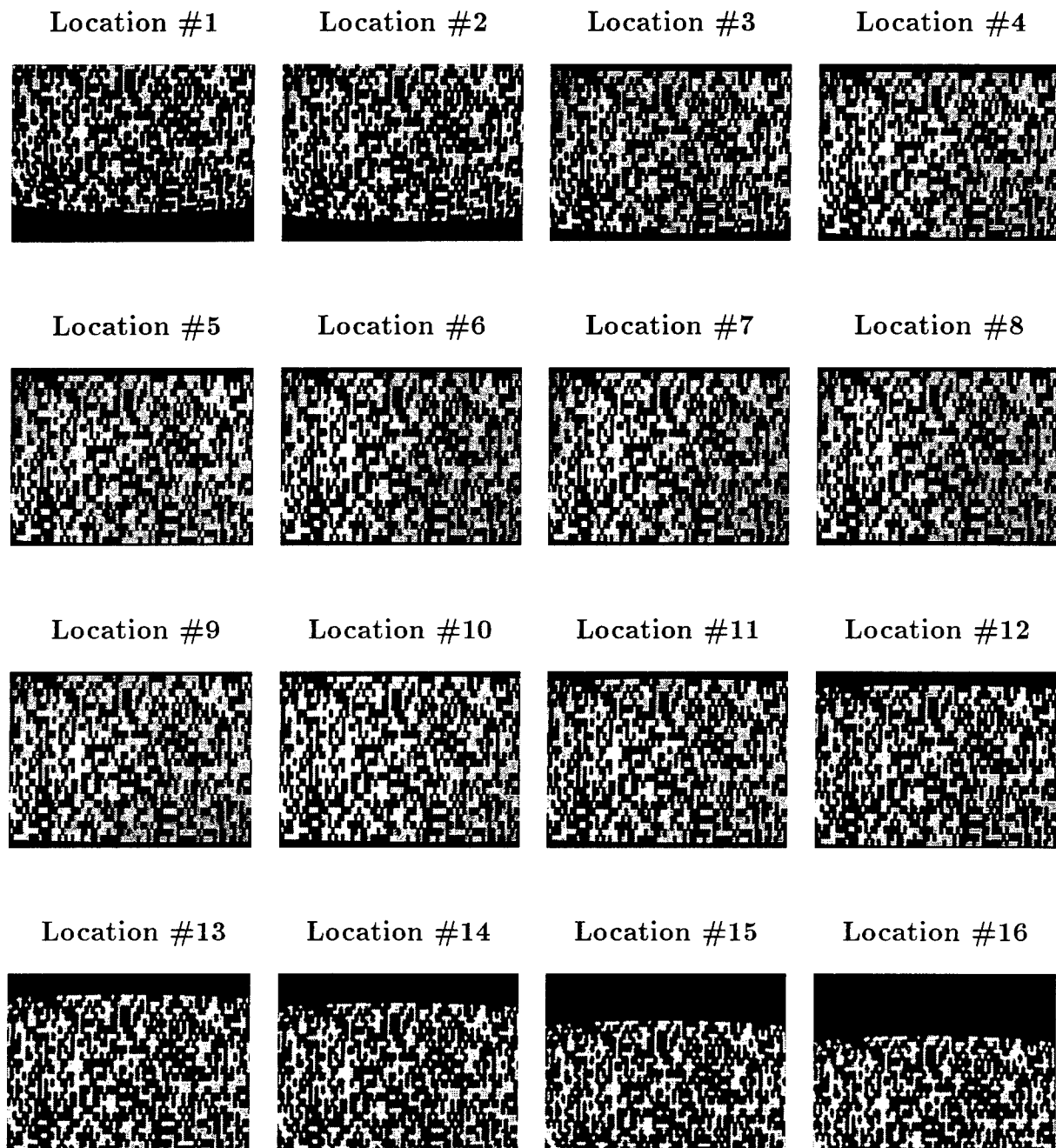


Figure 12: Storage of holograms in 16 locations: poor imaging system

vertical extent of each storage location. This parameter is the crucial sticking point: will each location be too small to capture the spatial frequencies of the image, or will the stack of locations be too tall to permit undistorted imaging of the SLM onto the CCD for all locations?

The magnification of the SLM influences three things in the object beam. We want to make the SLM image appear small so we can use many fractal rows, and also so we can fit the SLM image through the aperture. However, we want the SLM image to appear large so its Fourier transform is small. We usually proceed as follows: we decide to use every n mirror strips as fractal rows. We then calculate the minimum required magnification. For instance, we would need to magnify the SLM by a factor of 0.3 in order to use every mirror strip. If we use every other mirror strip, we could magnify by a factor of 0.6. In view of the problem discussed in the next paragraph, we settled on a magnification factor of 0.333 so that the SLM image would be smaller when it passed through aperture A_{object} . As one can see in Table 1, this choice made the Fourier transform quite a bit larger than the spot size, causing loss of some spatial frequencies.

This first design used $f_{object} = 300\text{mm}$, a computer-optimized achromat lens of 82mm clear aperture. A matched lens placed beyond the exit of the crystal to complete the 4-F system. These lenses had excellent performance over most of the clear aperture. However, the stack height of 6.7cm, consisting of >80% of the vertical clear aperture, proved to be too large for these lenses. This can be seen in Figure 12, where we show holographic reconstructions for storage in 16 locations. The center 10–12 locations or so show good imaging—however, the locations which use the extreme edges of the lens show unacceptable aberration and image loss.

At this point, we had three choices to correct this 16 location problem. We could have chosen to:

1. Obtain custom designed lenses of large aperture.
2. Shrink the size of the stack of 16 locations by reducing the focal length of the output lens f_{out} . We would also get the same effect through a redesign of the mirror array tilt angles, but we preferred to use our existing mirror array.
3. Use phase-conjugate readout to limit the clear aperture required of the signal beam lenses.

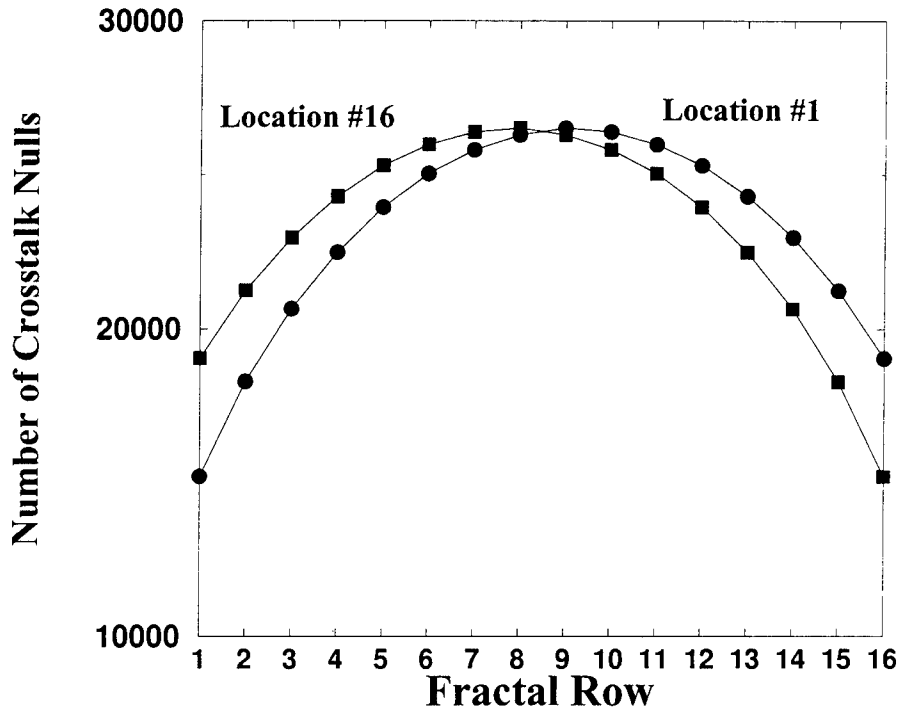


Figure 13: Maximum number of angle-multiplexing nulls allowed by the aperture of the quarter-waveplate

In our experiment, we chose to use Option 2. We describe the design here, and show the experimental results in the next section.

We reduced the focal length of the reference beam lens L_1 from 120mm to 70mm, as shown in Table 1. With this change, we can use a pair of f=200mm, 70mm aperture achromats in the object arm. The advantage of moving to a shorter f_{object} is that the size of the Fourier transform spot decreases, which we really need because the vertical spacing between each location has also shrunk. Since the aperture A_{object} was no longer a problem, we could use a magnification ratio that just allows us to use every other mirror strip ($n=2$). From Table 1, the Fourier transform of the object beam is still larger than the spacing between locations, but the discrepancy is much smaller.

Given these lenses and apertures, we can determine how many of the 256 mirror strips are accessible to us, and how much angle multiplexing bandwidth we have on each. We will assume that we'll be using a 2 inch cubic beamsplitter, a 2 inch circular quarter-wave plate with 1cm of clearance

between the waveplate and the mirror array, and a Fresnel lens with 7cm focal length and a 7cm square aperture. The quarter-waveplate has a more involved effect than the others, since it alone has a circular aperture. We show the maximum number of angle-multiplexing nulls in Figure 13 if the waveplate were the only limiting factor. As expected, the angle multiplexing range is smaller for the mirror strips which lie at the edges of the mirror. The curves are not symmetric because of the tilt of the mirror facets—at one end of the mirror array, light is directed back towards the optical axis where the waveplate is wider. At the other extreme of the mirror array, light is directed away from the optical axis and fewer angle multiplexing nulls are available. We have assumed that the angular selectivity is

$$\frac{\lambda}{L} = 2.44 \times 10^{-5} = \frac{1.7\mu m}{70mm}.$$

The theoretical angular selectivity increases as the reference beam moves away from normal incidence. In practice, however, the measured angular selectivity is usually broadened considerably by the non-plane wave nature of the reference beam. This is especially true when using a Fresnel lens, as the reference beam may be composed of multiple spherical waves. However, angular selectivity continues to operate, as long as the radius of curvature of the spherical wavefront is much larger than the interaction length of the hologram. In terms of our analysis of the capabilities of our reference arm, we need to space the holograms further apart within the same horizontal deflection range. The non-plane wave reference beam reduces the number of angle-multiplexing nulls.

So far, we have only discussed the limitation on the reference beam imposed by the aperture of the quarter-waveplate. The beamsplitter and Fresnel lens impose an additional limitation on both vertical deflection and horizontal angle-multiplexing bandwidth. However, since these two apertures are square, the horizontal and vertical effects are not coupled. The 2 inch beamplitter limits the angle-multiplexing to 15,100 nulls, and the Fresnel lens to 17,650 nulls. In addition, beams from some of the mirror strips do not clear the aperture of the beamsplitter. Only the extreme locations: 1, 2, 15, and 16 are affected. The bottom 4 mirror strips which are pointed at location 1 are blocked, as are the top 4 mirror strips pointed at location 16. This makes sense, as the light leaving these mirror strips starts far from the optical axis and is deflected farther by the tilt of the mirror strip. No surprise that the beams never get out of the far end of the beamsplitter. For

locations 2 and 15, the two extreme mirror strips cannot be used.

Even though the reference beams pass through all of the apertures, they still may be unusable. If the vertical dimension of the beam is shrunk by off-axis aberrations, it may fail to overlap all of the information the signal beam. If the horizontal dimension shrinks, then we can still use the reference beam if we compensate for the reduced diffraction efficiency and angular selectivity.

3 Holographic Random–Access Memory: Experiments

In this section, we experimentally demonstrate the various elements which compose our holographic random access memory. We start by demonstrating spatially multiplexed storage in 8 locations using the mirror array. We then demonstrate storage of 1000 angle–multiplexed holograms using an AOD in the reference arm with an EOM in the signal arm. This corresponds to one fractal row of our 160,000 hologram system. Returning to mechanical scanners, we store 10,000 holograms in a single location ($\sim 1\text{cm}^3$) using the image plane and then the Fresnel plane geometries. We then demonstrate storage in 16 locations using the mirror array, and use the full system to store 10,000 holograms at the top, center, and bottom locations. Finally, we conclude with some related experiments which we performed, including using the mirror array system for simultaneous memory readout and real–time face correlation, and thermal fixing of multiple holograms.

3.1 Storage using the mirror array

The 90° geometry—with reference and signal beams entering orthogonal crystal faces—was used to angularly multiplex up to 500 holograms at each of 8 spatially multiplexed locations in a LiNbO_3 crystal. The segmented mirror array and a 2-D mechanical scanner were used to perform both angular and spatial multiplexing.

The experimental setup is shown in Figure 14. The recording medium was a 0.01% Fe-doped LiNbO_3 bar of dimensions $8\text{mm} \times 8\text{mm} \times 50\text{mm}$, cut for the 90° geometry. Holograms are recorded with the signal beam propagating down the long axis of the bar and the reference entering from the side. This configuration is convenient: since the signal beam is present at all spatial

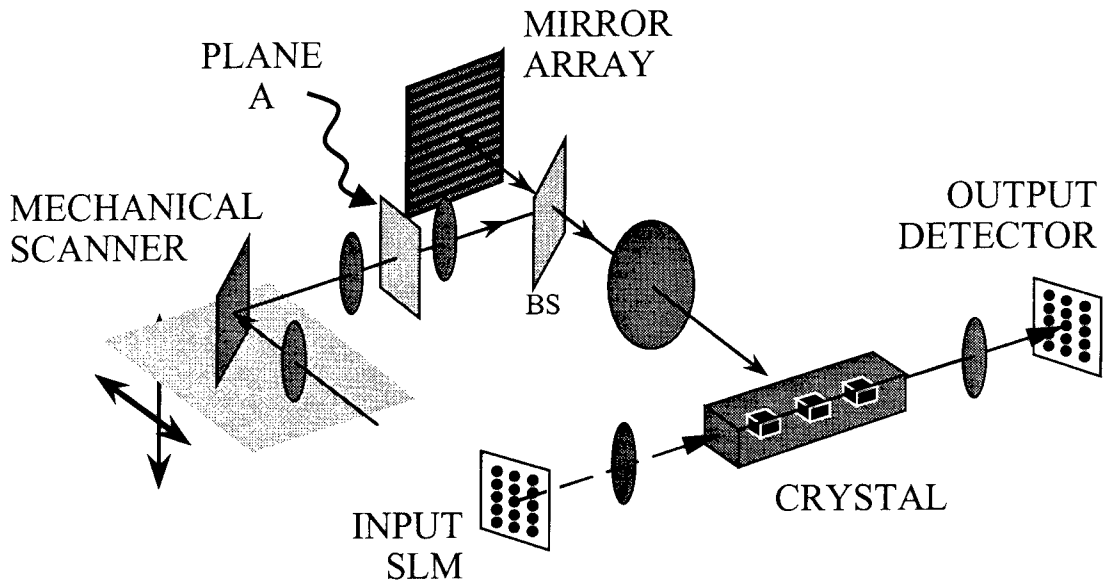


Figure 14: Spatially–multiplexed storage using the mirror array

locations, there is no need to deflect the object beam. Input images were presented on a fixed input SLM and reconstructions observed on a fixed 2-D CCD array at the other end of the bar, no matter which location was being accessed. In this experiment, the SLM was a transparency mounted on a rotational stage.

The reference arm consisted of a mechanical scanner, a segmented mirror array, and several lenses. The scanner focused the input beam to a spot with a single lens and reflected the light off a mirror oriented at 45° with respect to the optical axis of the lens. The position of the focused spot could be scanned in both dimensions by moving the lens and mirror assembly with two computer-controlled actuators. Note that horizontal translation was achieved by moving the assembly in the axial direction, so there was no limit on movement in this dimension. A periscope arrangement can be used to achieve the same effect in both dimensions, but was not necessary in this experiment. A pair of lenses imaged the focused spot onto the mirror array. As described in the previous section, the 2-D movement of the focused spot on the mirror array implements both spatial and angular multiplexing at the crystal.

First, 500 holograms were stored at a single location with a 6mm diameter

reference beam. An exposure schedule was used to equalize the diffraction efficiencies of the holograms. The longest exposure was 12.2 seconds and the shortest 1.65 seconds. The total recording intensity incident on the crystal was 130 mW/cm^2 , the ratio of the reference to signal beam intensity incident on the crystal was 6.25, and the average diffraction efficiency 10^{-8} . Several reconstructions are shown in Figure 15. The original transparency is shown at upper left, and was rotated 1° between each exposure.

Next, holograms were recorded at each of 8 spatially multiplexed spots (each reference beam was 4mm in diameter) along the length of the crystal, using 8 of the 256 mirror strips on the mirror array. At locations near the center of the crystal, 500 holograms were stored at each location. Towards the ends of the bar, the limited aperture of the beamsplitter restricted us to 350 holograms per location. The average diffraction efficiency was again 10^{-8} . Several reconstructions are shown in Figure 16. Note that, in the reconstructions of the holograms stored towards the ends of the bar, the top and bottom edges are missing. This occurred because the reference beam becomes oval-shaped at these outermost storage locations, due to lens aberrations and the inclination of the mirror strip out of the focal plane as the focused spot moves off-axis.

In our experiment, the limit on the number of holograms per location was the number of distinct reference angles we could provide to each location, rather than crystal dynamic range. This limit was imposed by the beamsplitter aperture, not the mirror array. We only used 28mm (about 37%) of the horizontal extent of the mirror array. Therefore, an optical system with larger apertures can access 1000 holograms per spot, or more. In this system, there were additional losses not normally encountered in a standard angle multiplexing holographic setup, bringing signal levels closer to the fixed detector noise floor and reducing dynamic range. These losses include the optical loss at the nonpolarizing beamsplitter, the low reflectivity (40%) of the gold surface of the mirror array, and absorption in the long crystal. Absorption allows approximately 5% of the light illuminating one of the end faces to be transmitted out the other end.

One final aspect to be considered is the presence of the object beam at all locations, including those where holograms have already been written. Holograms at the location which is first used for storage will be erased by the object beam during exposure of all subsequent holograms. This does not cause much difficulty in the system described above for two reasons. One reason is that the external ratio of reference to signal intensity was large

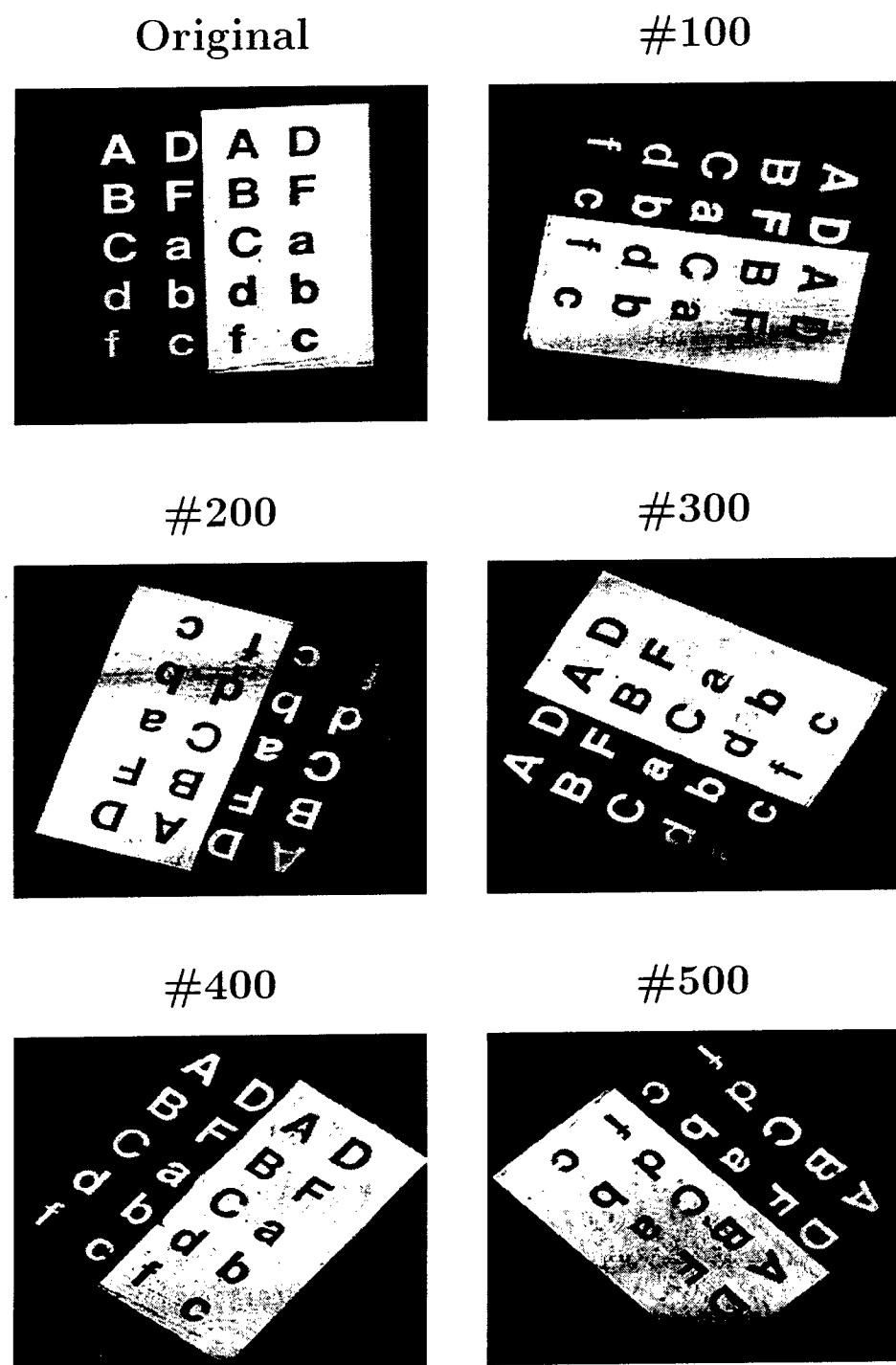
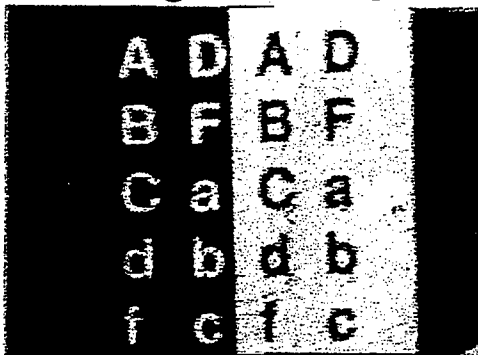


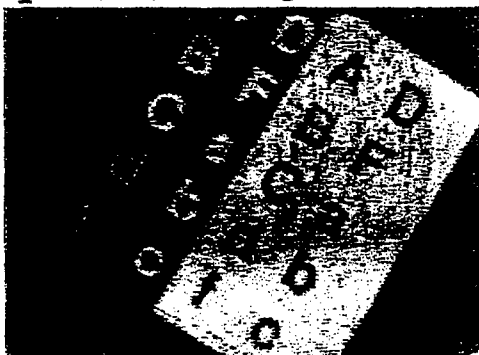
Figure 15: Example reconstructions: storage of 500 holograms at one spot.

8 Spots—500 Holograms each

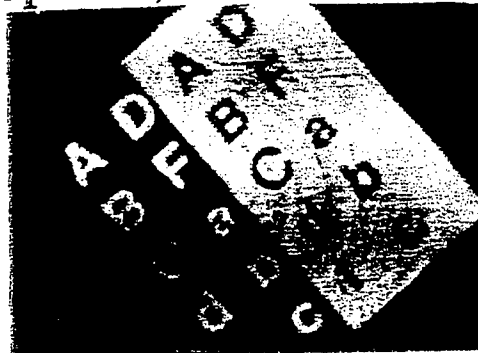
Original Image



Spot #2, Hologram #200



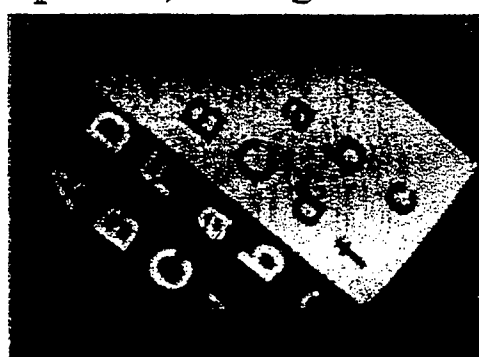
Spot #3, Hologram #300



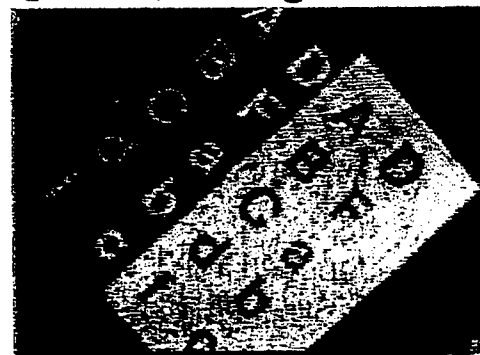
Spot #7, Hologram #200



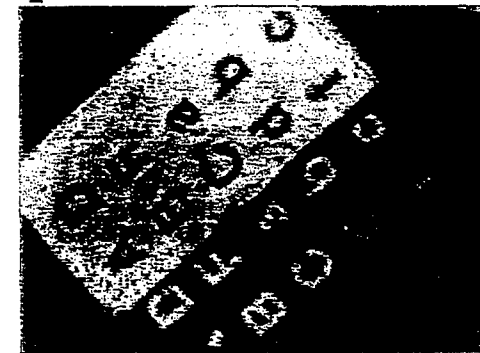
Spot #1, Hologram #400



Spot #2, Hologram #400



Spot #4, Hologram #200



Spot #8, Hologram #200

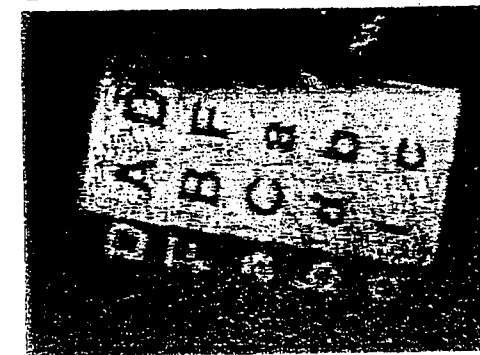


Figure 16. Example reconstructions from storage of 500 holograms at each of 8 spots.

(approximately 6.25). In addition, the storage locations can be filled starting from the end farthest from the entry of the object beam. In this way, the holograms exposed to the object beam for the longest time are buffered from its effects by the absorption of the long crystal. For these two reasons, very little erasure of the holograms occurs once the reference beam moves to the next storage location.

In the experiment described above, we used a mechanical scanner to move a focused spot and a pair of lenses to image this moving spot onto the surface of the mirror array. In the center of this pair of lenses (plane **A** in Figure 14), there exists a plane wave centered on the optical axis with a vertical and horizontal incidence angle. We can create an identical plane wave by using a 2-D non-mechanical angle scanner in this plane **A**. One such example is a pair of crossed AOD cells with cylindrical accessing lenses. The Doppler shift added by these cells can be removed by an electro-optic modulator (EOM). In this way, the mirror array can provide spatially multiplexed holographic storage without mechanical movement. In the next section, we demonstrate holographic storage using one AOD and an EOM for frequency compensation.

3.2 Storage using an AOD

We used the 90° geometry to demonstrate storage and readout of holograms using an AOD and a compensating EOM. The experimental setup is shown in Figure 17. The reference arm is a 4-F system which images the angle change from the AOD onto the crystal. A block in the center Fourier transform plane spatially filters the DC or undeflected light. We used a Crystal Tech: AOD4050-2 TeO₂ slow shear AOD with a center frequency of 50MHz and an acoustic velocity of 617 m/sec. The angle deflection is proportional to the driving RF frequency. For the full frequency range from 33Mhz to 66Mhz, we obtained a deflection of 1.5°. The 5:1 4-F system demagnified the 4cm illuminated aperture of the AOD to a 0.8cm wide beam at the crystal, and expanded our angle deflection range to 7.5°. The measured and expected angle selectivity, represented in terms of RF frequency, are shown in Figure 18. Since the reference beam was apodized by the AOD aperture, the selectivity function no longer has visible nulls. We stored 1000 holograms by using a inter-hologram spacing of 30kHz. By using a quarter-wave plate both before and after the AOD, we were able to achieve an peak efficiency of 86% at the center frequency. However, in order to have uniform efficiency across the tuning range, we detuned these waveplates to obtain a uniform response of

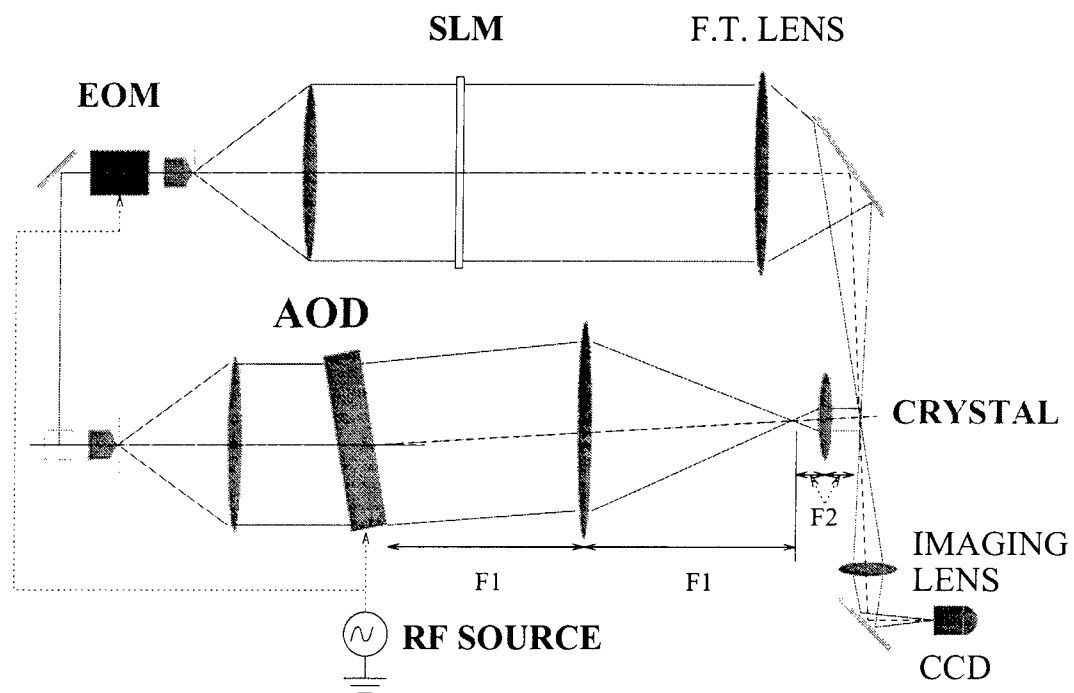


Figure 17: Storage of 1000 holograms using an AOD: experimental setup.

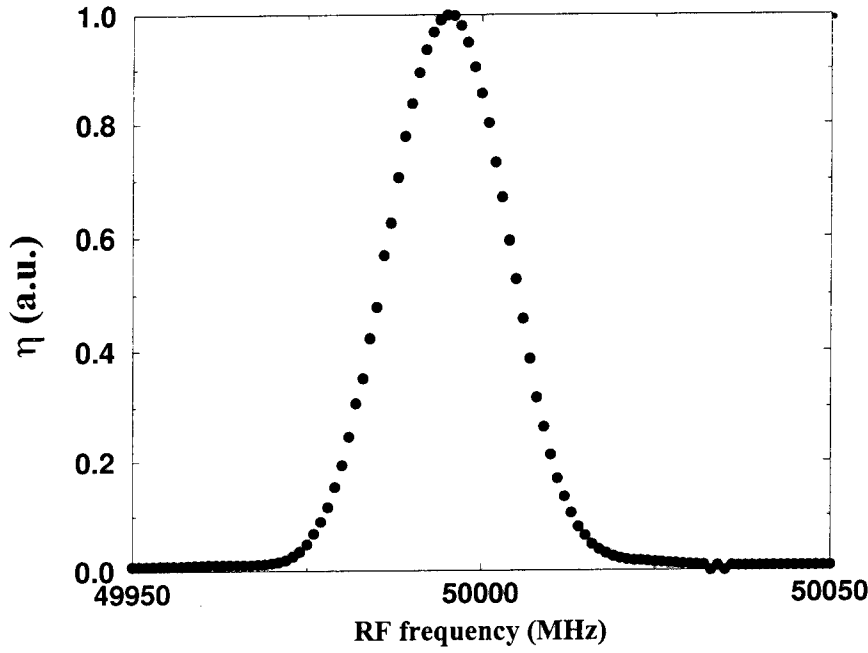


Figure 18: Measured and expected angle selectivity, in terms of RF frequency.

22%. The main purpose of doing this was to simplify the exposure schedule as much as possible.

The signal beam contained a New Focus Model 4002 broadband electro-optic modulator using Mg-doped LiNbO₃. This device operates on the “raw” laser beam and outputs an undeflected phase-modulated beam containing many spectral orders. The signal beam was then expanded, illuminated the SLM, and directed to the crystal. The crystal was placed just in front of a Fourier transform plane of the SLM image (Fresnel plane storage). In this experiment, the SLM consisted of a slide which was rotated several degrees between each exposure.

The phase-modulated beam can be described as:

$$e^{j\omega t} e^{j\delta \cos \Omega t} = e^{j\omega t} (J_0(\delta) + J_1(\delta)e^{\pm j\Omega t} + J_2(\delta)e^{\pm 2j\Omega t} + \dots) . \quad (14)$$

Only one of these terms ($e^{j(\omega+\Omega)t}$) corresponds to the Doppler-shifted reference beam, so efficiency and modulation depth are serious concerns in this system. The parameters that we can control are δ and the input polarization. We are also free to use any output polarization, since we can use a half-wave

plate to return the signal beam to the vertical polarization we need for the 90° geometry. Our optimization goal is not obvious, as we need to increase the amount of light modulated by the correct order, as well as minimize the amount of light remaining in the unmodulated zero order. The exact determination of the configuration depends on the relative importance of these two parameters. In our experiment, we achieved 45% modulation into the first-order with 10% of the power remaining in the zero order. Note that there exists, corresponding to the useful plus one order, an equally efficient yet useless minus one order. The waste light reduces modulation depth and $M/\#$. In the AOD system, we obtained an $M/\#$ of 0.28; in contrast, the same crystal crystal, with 0.01% Fe doping, achieved an $M/\#$ of 0.8 for holograms stored without an AOD. As a result, the diffraction efficiency of the AOD-stored 1000 holograms was $\sim 8 \times 10^{-8}$.

The reconstructed holograms were measured with a Photometrics Imagepoint CCD array containing an 8-bit digitizer—some reconstructions are shown in Figure 19. The detector pixel map covering the image (310,000 pixels in all) was divided into regions which were expected to be bright (or dark). In this process, “edge” pixels near a dark/bright transition were discarded. The two resulting histograms are representations of the probability density functions (PDF) for storage of binary data in this system. The two PDFs are shown in Figure 20 for a sample reconstruction—approximately 200,000 pixels from the image are represented in all. An optimal threshold was empirically determined, giving a measured raw probability of error of 10^{-5} . We could reduce the measured error to zero by using one threshold for the center portion of the image, and a different one for the edges.

3.3 Storage of 10,000 holograms

10,000 image plane holograms Using the system shown in Figure 21, we stored 10,000 image plane holograms in an $8 \times 8 \times 50$ mm bar of 0.01% Fe-doped LiNbO₃. The c-axis was again cut for the 90° geometry, at 45% to the vertical faces. The reference beam was 45mm \times 5mm in area, and the object beam 4mm \times 5.4mm for a total interaction volume of 0.972 cm³. Images were presented on a liquid-crystal SLM from a projection television. The SLM was demagnified by a factor of 5 and imaged to a plane located approximately halfway along the long dimension of the crystal. Each hologram contained 480 \times 440 pixels, so that assuming one bit per pixel, 2.11 GBits were stored. Using a final exposure of 0.21 seconds and an erasure

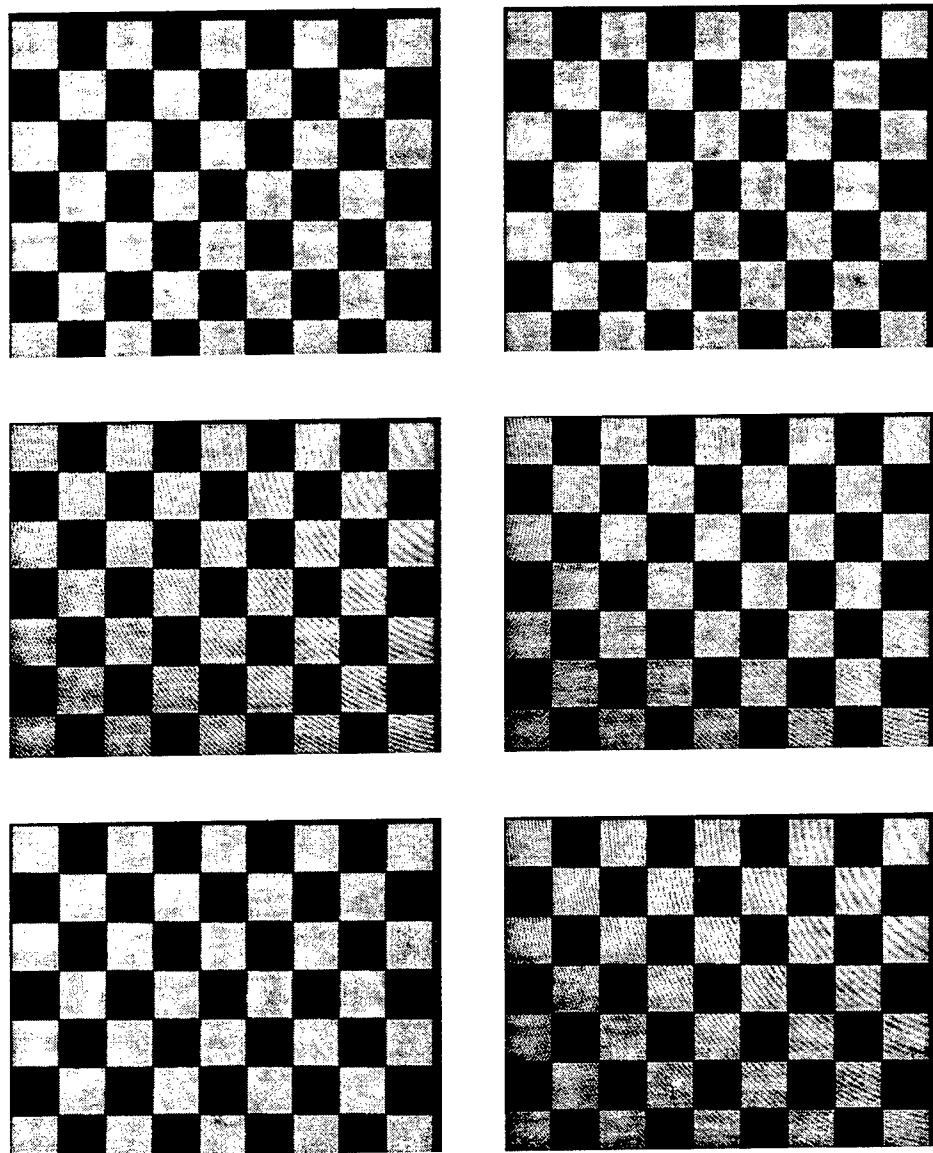


Figure 19: Storage of 1,000 holograms using an AOD: reconstructions.

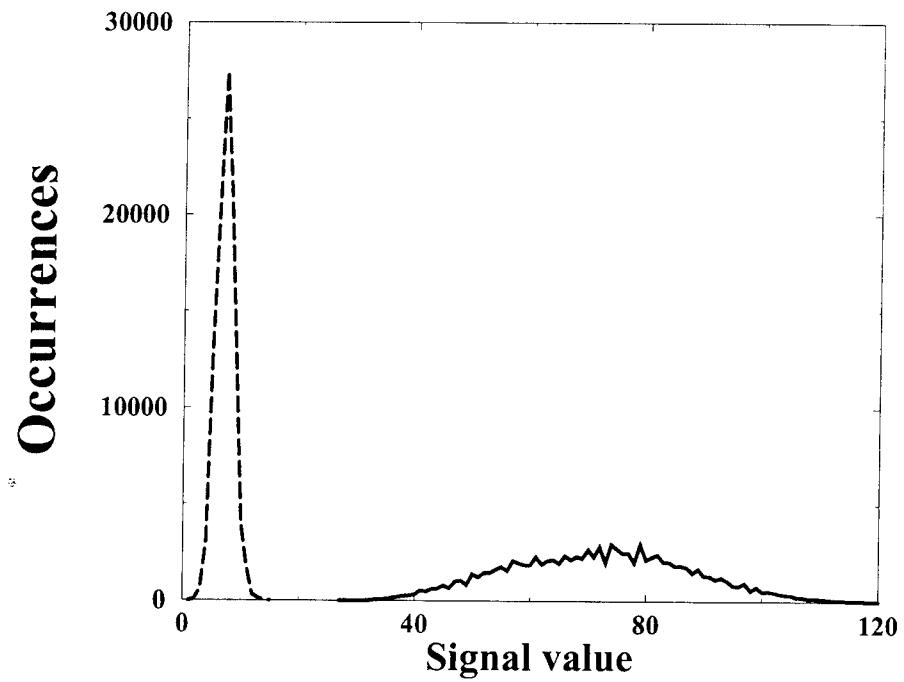


Figure 20: Probability density functions for ON and OFF pixels.

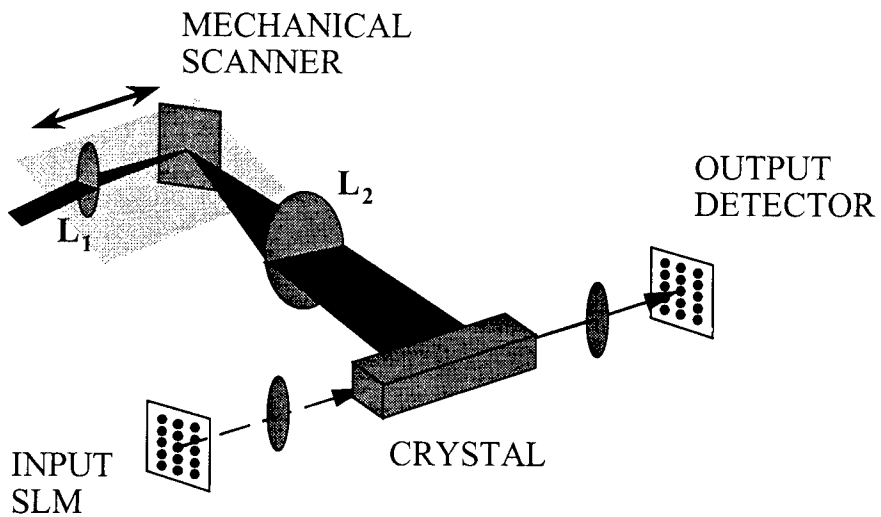


Figure 21: Storage of 10,000 image plane holograms: experimental setup

time constant of 2250 seconds, a standard recording schedule was computed. This led to an initial exposure of 3.1 seconds and a total exposure time of 102 minutes. The average exposure time was 0.61 seconds. The actual time required to complete recording was significantly longer since we included extra delays between each exposure for the mechanical scanner and video input to stabilize.

A 4-F system was used to magnify and image the reference beams onto the long face of the crystal, with a mirror at 45° near the center focal plane to fold the optical axis by 90° (See Figure 21). Lens L_1 and the mirror were fixed relative to each other and mounted on a linear actuator capable of 4 inches of travel parallel to the incoming reference beam, while lens L_2 and the crystal were mounted on the optical table. By moving the linear actuator back and forth, the focused spot at the folding mirror was translated horizontally in the back focal plane of lens L_2 . This translation appeared at the crystal as a change in the horizontal incidence angle of the reference beam, enabling angular multiplexing.

The experimentally measured selectivity of 1.1×10^{-5} radians (all angles external to the crystal) agreed with theoretical expectations for the 90° geometry and a 45mm interaction length. Although the presence of images broadened the effective selectivity by a factor of 2 or so, a spacing of 4×10^{-5} radians was sufficient to suppress holographic readout by about 30dB. To implement this spacing with a lens L_2 of focal length 150mm, the linear actuator was moved $6\mu\text{m}$ between holograms for a total travel of 60mm.

The input images during the experiment included gray-scale cartoon images as well as a benchmark chessboard pattern. Several reconstructions of this chessboard pattern are shown in Figure 22. You can see the effects of non-uniformity of the signal and reference beams, in the loss of fidelity at the corners of the output images. The hologram number appears in the upper left corner of each hologram. As can be seen, the time constant used was slightly too high, and the early holograms decayed more than expected. The average diffraction efficiency of the chessboard images was measured to be about 5×10^{-9} , so the power in the reconstructed holograms was within the same order of magnitude as the background light scattered by the crystal. Fanning of the reference beam did not appear to affect storage.

At this point, we can store 10,000 holograms at each location. Incorporating the SLM limits, the total achievable storage capacity at one location is between 1 and 10 gigabits. In order to increase the total capacity beyond this limit, we can use spatial multiplexing. If we continue with image plane

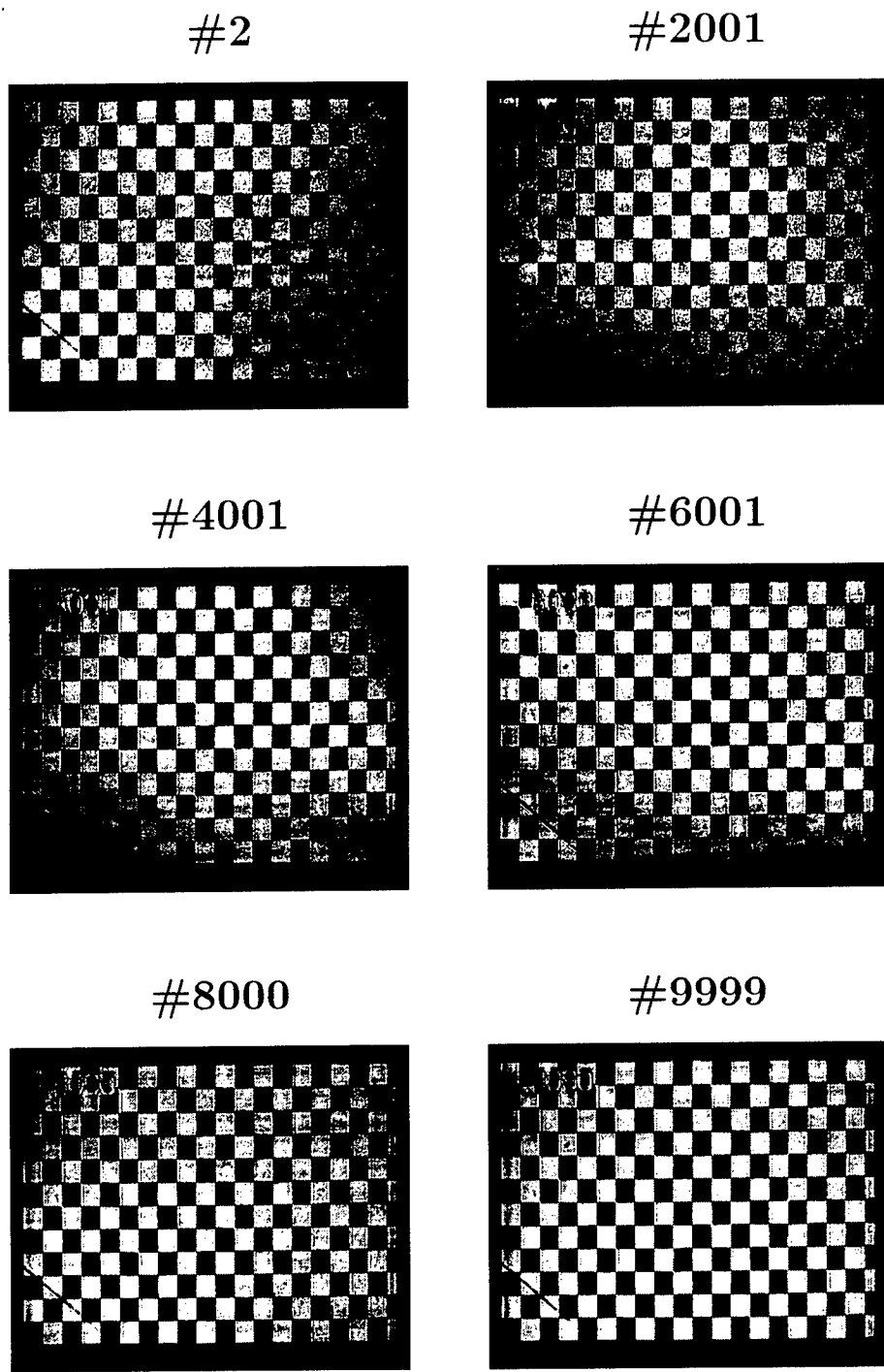


Figure 22: Storage of 10,000 image plane holograms: reconstructions.

storage however, we will need to move the array detector to access holograms from different locations. However, by storing Fourier plane holograms, we can detect the reconstructed holograms from multiple locations without moving the detector array. We can obtain the same effect by storing in a plane slightly away from the Fourier plane, which we usually refer to as Fresnel plane storage.

10,000 Fresnel plane holograms In this section, we describe the storage of 10,000 holograms in one storage location of a $\text{LiNbO}_3:\text{Fe}$ crystal using near-Fourier plane storage. Figure 23 shows the experimental setup. The reference arm contains an XY mechanical scanner which moves the focused reference beam horizontally for angle multiplexing, and vertically for fractal multiplexing. You can think of this setup as corresponding to one location of the 160,000 hologram system, where multiple identically-tilted mirror strips access the same location. Not shown in the drawing are two cylindrical lenses which magnify the horizontal dimension of the reference beam, and two mirrors in a periscope arrangement to convey this beam onto the mechanical scanner. Lenses L_1 and L_2 had focal lengths of 80mm and 120mm, respectively. The reference beam spot size was elliptical, about 20mm wide and 6mm high, with an area of 0.95 cm^2 .

The object beam is directed to the proper location after the image information has already been imposed on the beam. The image presented on the liquid-crystal SLM is demagnified by $3\times$ and imaged to a mirror mounted on a rotation stage. This horizontal deviation is not required in the theoretical design of our large-scale system, but it has an important role in its practical realization. One of the difficulties of storage in the LILA geometry is that as the amount of fixed pattern energy² increases, images become increasingly distorted. If we deflect the signal beam horizontally, these noise gratings do not build up as fast. In addition, although these holograms are all stored at the same vertical location, we have used additional crystal volume for storage, which will us increase the diffraction efficiency of the holograms.

The image plane in the center of this horizontally rotating stage is imaged via a 4F system to a pair of mirrors in a periscope arrangement. These two mirrors are used in the full system to deflect the signal beam vertically—in this experiment, they remained stationary. On the far side of lens L_3 (focal

²from dust, fixed patterns on the SLM display, or common features among the presented images.

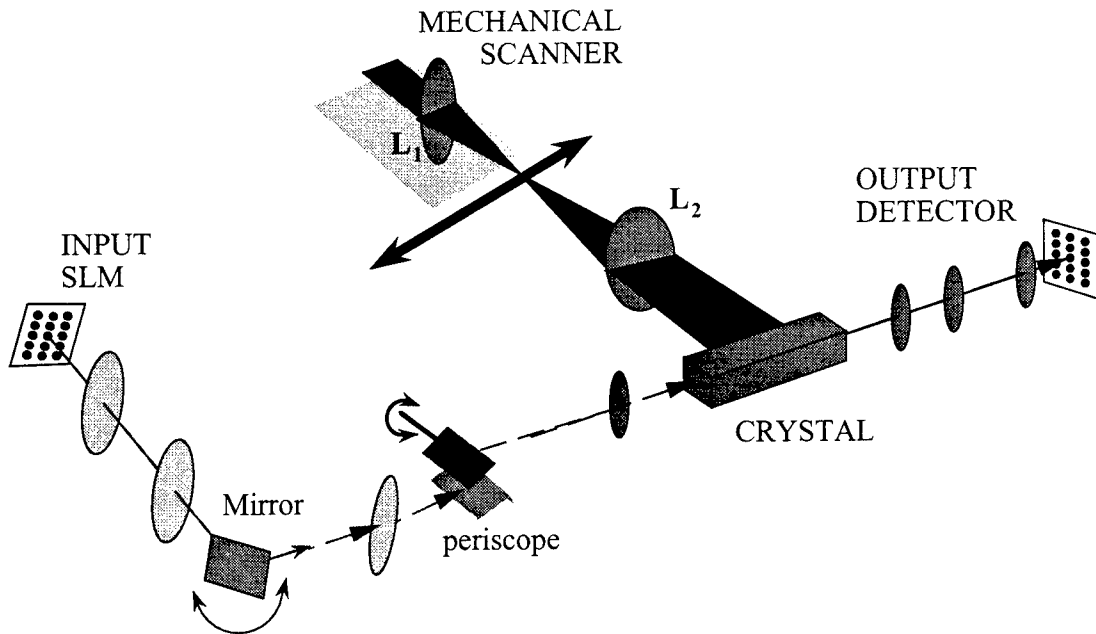


Figure 23: Storage of 10,000 Fresnel plane holograms: experimental setup

length 300mm), the horizontal angle determines where the Fourier transform of the displayed information arrives. Since a random phase plate was not used, the crystal was not placed in the Fourier transform plane, but was displaced beyond it by 80mm. At this point, the DC portion of the expanding image was approximately 1.77mm high \times 2.4mm wide. Three lenses after the crystal filter out scattered light and magnify the reconstructed images onto a Photometrics Imagepoint cooled scientific CCD. The advantage of Fourier transform storage becomes apparent at this point, since a reconstruction from any spot in the crystal can be imaged onto the single detector array.

10,000 holograms were stored in a 0.01% Fe-doped crystal bar of dimensions $10 \times 10 \times 20$ mm. The c-axis was at 45° to the vertical faces. The images were displayed on a 640×480 pixel VGA monitor, and sampled for the 480×440 pixel SLM. Both random bit patterns and a standard chessboard pattern were stored. The last exposure time was 0.26 second and the erasure time constant was 3800 seconds. The initial exposure lasted 7 seconds, the total exposure time was 134.6 minutes, and the average exposure time 0.81 seconds. Four fractal rows were used for storage with 2500 holograms stored on each. The vertical spacing between fractal rows was 5mm (1.4°); the hor-

izontal spacing between holograms was $15\mu\text{m}$ (.004°). The angles listed are the external angles at the crystal face. The vertical angular bandwidth of the images was 1.15°, so the fractal spacing completely displaced unwanted reconstructions off the detector array. Several reconstructions are shown in Figure 24. These images were taken with exposure times between 0.5 and 1 second.³ The average diffraction efficiency was approximately 5×10^{-9} . The average power in the reconstructions (which were already half dark) was 2.5 times the background scatter (measured before storage).

Compensation of the background illumination profile To characterize the noise performance in this angle multiplexed memory, we normalized the reconstruction by an overall illumination profile. This allows us to significantly suppress deterministic sources of errors, such as beam nonuniformity and dust particles on the optical components. Such deterministic error sources, common in a research-grade system, can in principle be eliminated by careful engineering. The performance we obtain after normalization provides an estimate for the performance that is expected from a prototype system.

As in the noise analysis described previously, several reconstructions of the chessboard images were captured with the detector array and digitized. The edge pixels were discarded, leaving two sets of detector pixels: ON pixels and OFF pixels. Each detector pixel is treated as a separate sample—there is no spatial averaging. The histogram of each set of detector pixels is a PDF. We can obtain several parameters from these two PDFs to describe the error performance of the holographic memory:

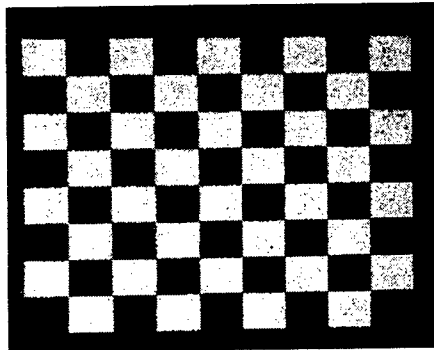
- the measured bit error rate or P_e . We determine the best measured P_e by empirical selection of the threshold between ON and OFF.
- the signal-to-noise ratio. We define SNR as

$$SNR = \frac{\mu_1 - \mu_0}{\sqrt{\sigma_1^2 + \sigma_0^2}}. \quad (15)$$

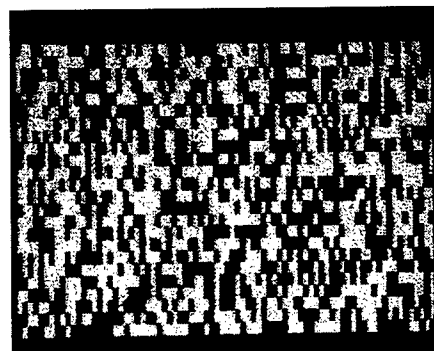
The SNR is a useful indicator of the error performance: a large SNR indicates a low bit-error rate.

³We could distinguish ON and OFF pixels with shorter exposures, but to have accuracy in measuring bit-error rate, we always tried to use the full dynamic range (8 bits) of the camera.

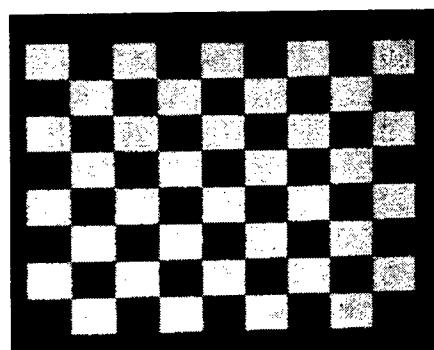
#1



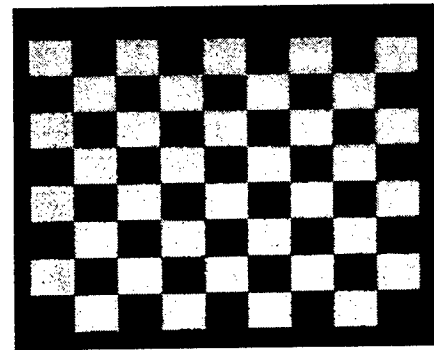
#2749



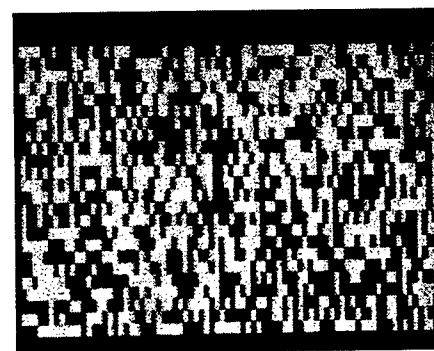
#3999



#5999



#7246



#9931

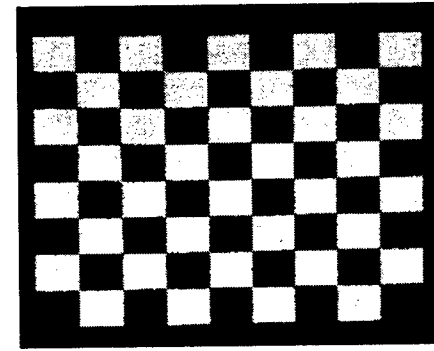


Figure 24: Storage of 10,000 Fresnel plane holograms: reconstructions.

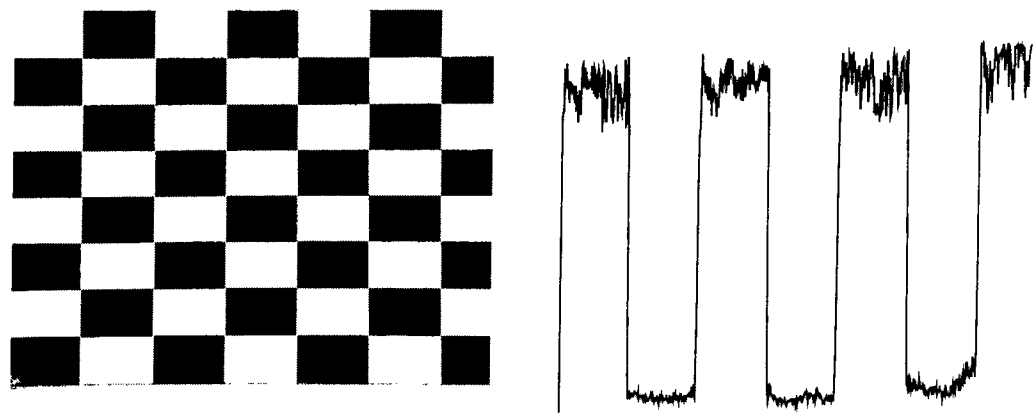
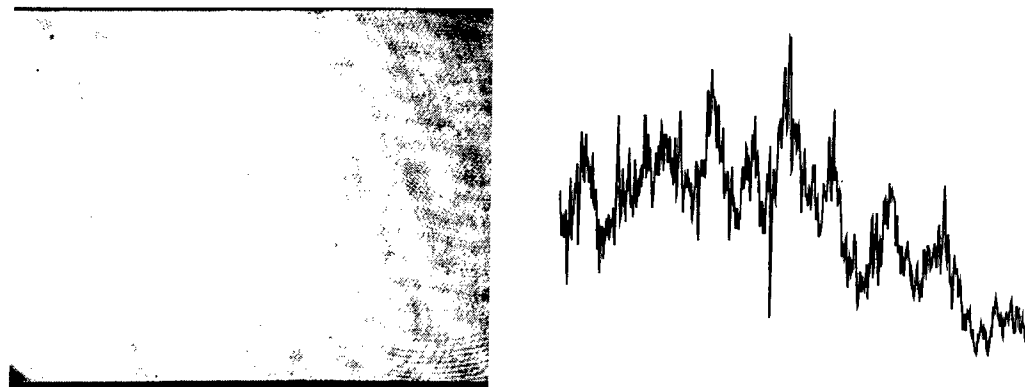
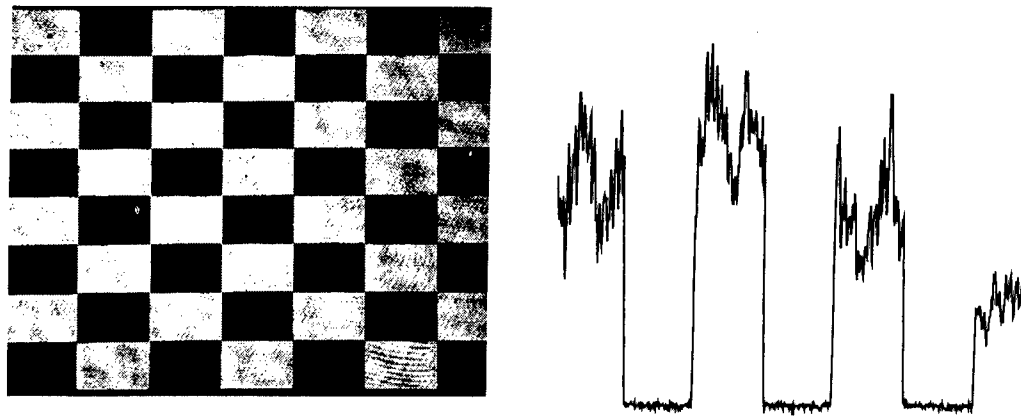


Figure 25: Normalization by the background illumination profile.

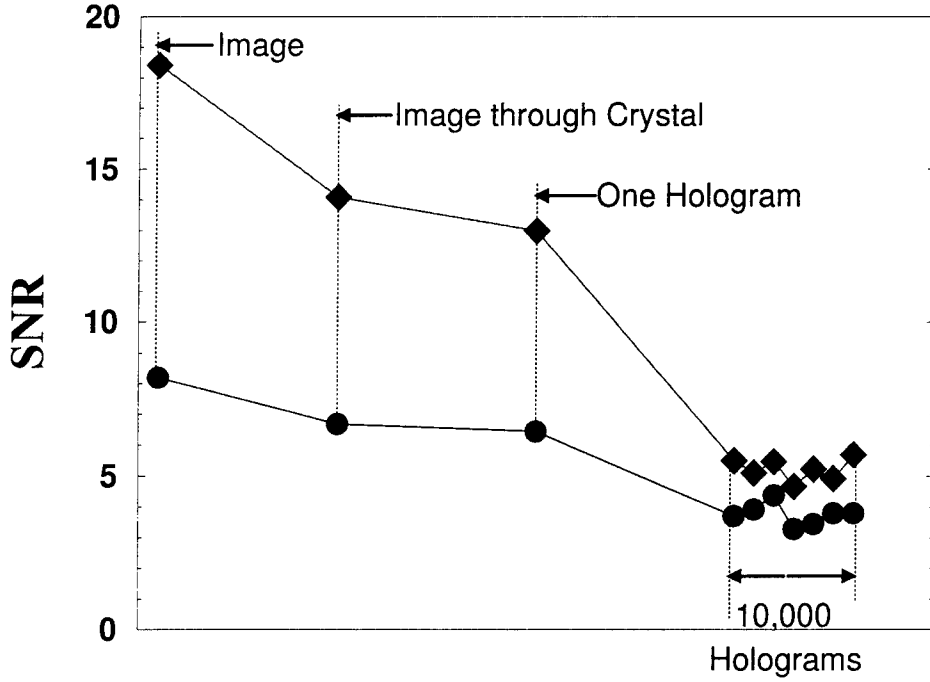


Figure 26: Evolution of the system SNR

- the estimated bit-error rate. We estimate the shape of the PDFs by assuming that they follow a particular distribution, such as the Gaussian distribution. This is often necessary if the error rate is smaller than the inverse of the number of samples.

The normalization procedure is pictured in Figure 25. On the top of the figure, we show the uncompensated reconstruction and a cross-section. In the center is the reconstruction of a hologram stored with all pixels ON. This blank page hologram is stored near the data hologram so that it has the same spatial profile. We then divide the data hologram by the blank page hologram. The profile is spatially smoothed and normalized so that the compensated data pattern has amplitude values in the same range as the original data. We show the compensated reconstruction and a cross-section at the bottom of Figure 25.

In order to see what noise was added by the holographic storage process, we analyzed the SNR of the images for several additional conditions. We captured images without the crystal present, for transmission of the signal beam through the crystal (no hologram), for storage of one hologram, and

storage of 10,000 holograms. Each chessboard image was also compensated by a blank page image as described above. The SNR for these various conditions is shown in Figure 26. The SNR after compensation is the upper curve; before compensation, the lower curve. Note that there is a degradation of SNR as the crystal is introduced and more holograms are stored, both with and without normalization. However, for the normalized images, there is a more pronounced difference between the SNR of the various test images and the SNR obtained when the 10,000 holograms are stored. This implies that the normalization procedure is more effective for imaging than for holographic reconstructions.

The SNR obtained in the absence of the crystal is principally limited by residual nonuniformity in the illumination and the SLM. The introduction of the crystal reduces the SNR because of surface defects and scatter noise in the uncoated crystal. Note that introduction of the crystal is the largest source of SNR loss in the system. The small reduction in SNR when a single hologram is stored is attributed to the nonuniformity of the reference beam and the spatially varying modulation depth. We have significantly reduced this variation in modulation depth by recording the holograms away from the Fourier plane. The final SNR, after storage of 10,000 holograms, is lower than the SNR from a single hologram. The reason is not loss of signal strength, because we made the single hologram measurement with the same diffraction efficiency as each of the 10,000 holograms. Instead we attribute the lower SNR to three factors: Crosstalk (adjacent holograms were recorded at the 3rd null of the angular selectivity curve), development of interpixel and other noise gratings over the long exposure sequence, and nonuniform erasure of the recorded holograms due to absorption in the crystal and the movement of the signal beam.

3.4 Demonstration of 160,000 hologram system

Demonstration of storage in 16 locations In this section, we demonstrate the full 160,000 hologram system. First we demonstrate storage in each of the 16 spatially multiplexed locations. The experimental setup is shown in Figure 27. It is similar to the setup for the storage of 10,000 holograms, with the additional incorporation of the mirror array. The same 2-D mechanical scanner with periscope is used in the reference arm. The focused spot is directed onto the surface of the mirror array with a large polarizing beamsplitter cube. A quarter-wave plate in front of the mirror array

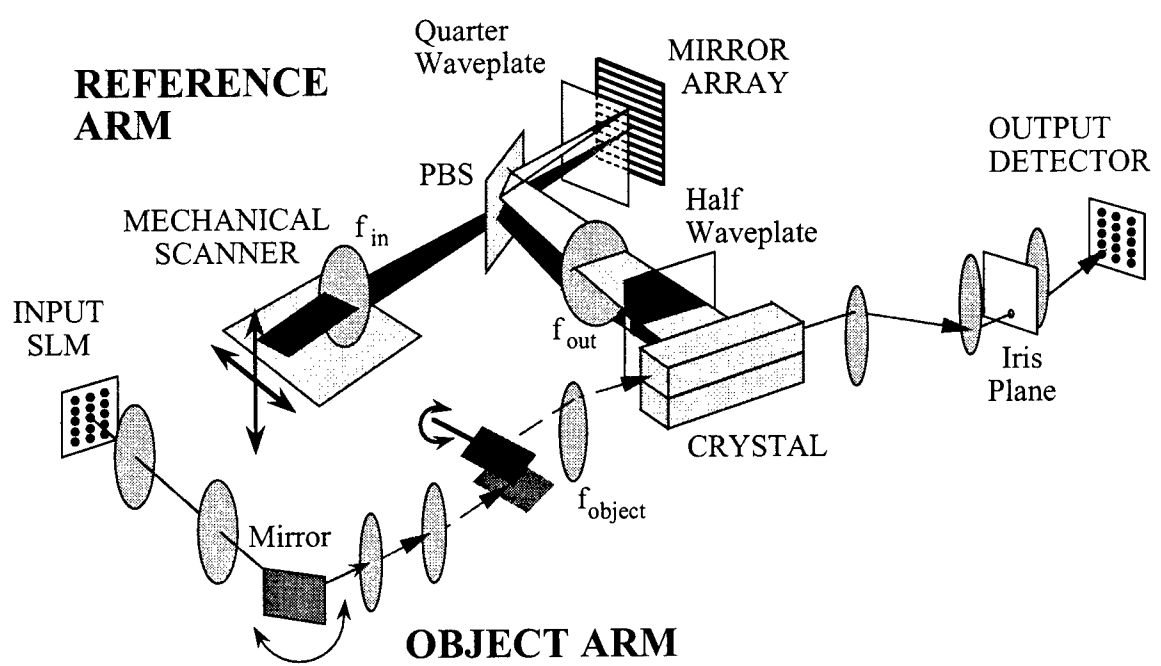


Figure 27: Experimental 160,000 hologram system.

makes both incoming and outgoing polarizations linear and orthogonal to each other. A half-wave plate in front of the crystal rotates the polarization to vertical, which we need for the 90° geometry. The overall efficiency of the beamsplitter/waveplate/mirror array combination is less than 25%.

We use the periscope in the image arm (described in the previous section) to perform vertical deflection of the signal for storage in the spatially multiplexed locations. The image plane in the center of the horizontally rotating stage is imaged to this pair of mirrors via a 4F system. The lower mirror is fixed and deflects the image by 90° to the upper mirror. The upper mirror is on a rotating stage, and returns the object beam to a near-horizontal path. The center of rotation of the upper mirror is in the second image plane of the object arm, and deflection originates from the optical axis of the lens f_{object} . At this point, the object beam has deflected by an arbitrary 2-D angle. On the far side of lens f_{object} , this angle determines where the Fourier transform of the displayed information arrives.

We used an $f_{object}=200\text{mm}$ achromat lens of 70mm aperture, and an identical lens after the crystal to complete the 4-F system. Using a .015% Fe-doped crystal of dimensions $2\text{cm} \times 1.5\text{cm} \times 4\text{cm}$, we were able to store holograms in 16 locations without loss of information, as we show in Figure 28. In Figure 29, we show SNR as a function of location for a single hologram in each location, and 1000 holograms in each location. The method for SNR analysis is described with the 30,000 hologram experiment below.

The top and bottom locations required a little refocusing and redirecting of the object beam for best focus and to maintain the reconstructions in the center of the camera. The need for this sort of adjustment implies that the distance between the lenses in the 4-F systems were not exactly correct, and that the rotation axes of the two deflecting mirrors were not positioned exactly in image planes of the SLM. We did not implement any refocusing with the array detector, but instead by translating lens f_{object} before storage. The readout optics then remained fixed and there was no effect on the readout speed. The lens f_{object} was moved within a range of 5mm for focusing purposes, and the vertical deflection mirror in our object beam periscope moved 1.6mm to center the images. Note that a slight rotation is seen of the vertically deflected images. This implies that the vertical deflection mirror also deflected the image horizontally a little. Another way of saying this is that the beams traveling in the vertical periscope did not lie in a single vertical plane.

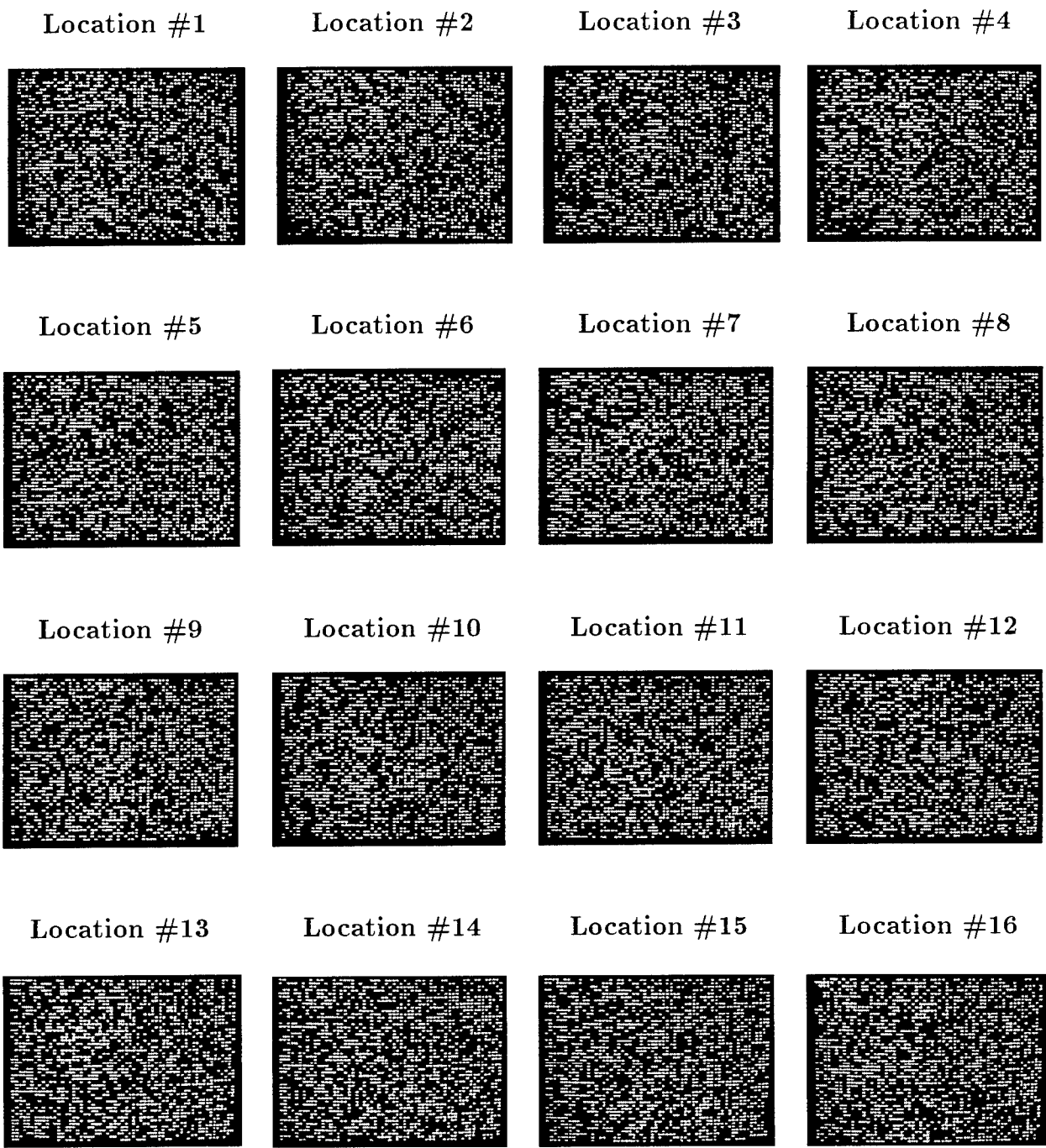


Figure 28: Reconstructions from 1,000 holograms at each of 16 locations

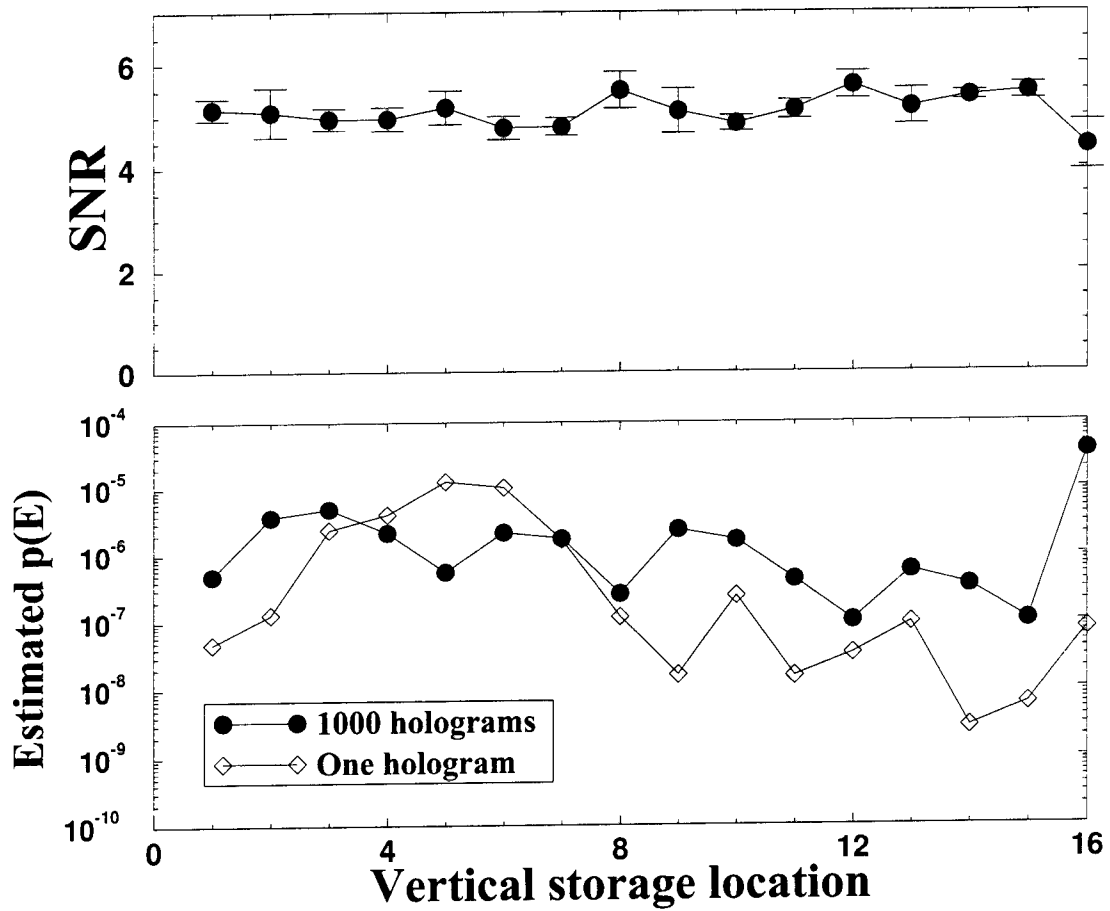


Figure 29: SNR as a function of hologram location.

Demonstration of storage of 30,000 holograms In order to demonstrate the full system, we used the same setup from Figure 27. In the previous section, we demonstrated the ability to deflect the signal beam to each of the storage locations and to get the reconstructions back to the array detector. Here we demonstrate storage of 10,000 holograms in the top and bottom locations, plus the center location for good measure.

Preparation of the reference arm —For this experiment, we needed to be able to use several mirror strips to implement the multiple fractal rows. However, some of the mirror strips that we would have liked to use were not available. The reason is that the mirror array was constructed as a stack of tiles which were then bolted together. In order to keep the total height of the mirror array from becoming too large, not very much tolerance was left between the outside mirror strips and the edge of the tile, which meant that when the tiles were assembled, some of these edge mirror strips became damaged or distorted. In some places this appeared as small blemishes; in others, an entire mirror strip would be unusable. These outside mirror strips, unfortunately, are exactly those which direct reference beams to the top and bottom location.

A second difficulty was the passage of the deflected reference beams from the mirror array to the crystal. As we mentioned in the previous section, the limited aperture of the lens f_{out} affects the number of fractal rows that we can use, as well as the range of multiplexing angles available in each fractal row. Each location has 16 mirror strips assigned to it, evenly distributed across the mirror array. As we would expect from our previous discussion, reference beams from the lower mirror strips work well if they are deflected towards the top location. This makes sense because they pass through the center of lens f_{out} , on the way from the bottom of the mirror array to the top of the crystal stack. Of course, because of the vertical size of the SLM, we must skip every other mirror strip when assigning fractal rows.⁴ As we use higher mirror strips, the reference beam passes through lens f_{out} farther from the optical axis and aberrations begin to distort the reference beam.

If we had used a plano-convex lens as lens f_{out} , we would have only had three fractal rows for angle multiplexing at the top and bottom locations. In

⁴If we were not to do this, then we would get three holograms overlapping at the detector array: one centered, one in the upper half of the screen, and one in the lower half of the screen.

order to reach our target of 10,000 holograms per location, we would have needed to store 3,333 holograms in each fractal row. However, the aberrations of the plano-convex lens also affect the horizontal deflection of the reference beam, adding complications to the spacing of the holograms. We were able to get around these difficulties by using a Fresnel lens of 70mm focal length and 70mm square aperture. The advantages were that our horizontal angle multiplexing range and the number of fractal rows increased dramatically. Even though the reference beam no longer resembled a single plane wave, we did not see any dramatic difference in angular selectivity. However, we did observe that we were unable to remove the crystal, reposition it in place, and find previously written holograms. This implies that the holograms correlate with the complex reference beam, and that any small shift in the crystal placement causes poor cross-correlation. As a result, we were unable to try fixing holograms that were written with the Fresnel lens.

With the Fresnel lens, however, we were able to use 4 fractal rows with 2500 holograms each, spaced at $10\mu\text{m}$ of linear translation.⁵ For comparison, the theoretical angle selectivity for a 1.8mm interaction length is 2.71×10^{-5} radians, or $1.9\mu\text{m}$ on the mirror array. The experimental angular selectivity we measured was around $5\text{--}6\mu\text{m}$ of movement, with vestigial secondary peaks. In justification of our angular spacing, we show the Bragg mismatching of one of 10,000 holograms in Figure 30. This sequence of images covers approximately half of the distance between the Bragg-matching condition and the next hologram ($5\mu\text{m}$). In Figure 31, we show the mean of the ON pixel regions, the optimum threshold, the SNR, and probability of error for these reconstructions. We describe the complete SNR analysis procedure later in this section. These two figures show that crosstalk was not a significant factor in our experiment.

Preparation of the object arm One of the main differences between the 10,000 hologram experiment described previously and this experiment was the vertical extent of the storage location. For the 10,000 holograms, we used a reference beam that was larger than the signal beam in order to guarantee overlap. (Of course, not too large or we would have wasted optical power and made our diffraction efficiencies seem poor). For the demonstration of the 160,000 hologram system, the height of the reference beam needed to be close to the vertical spacing between locations, or about 3mm. Our

⁵Translation of the focused spot on the mirror array.

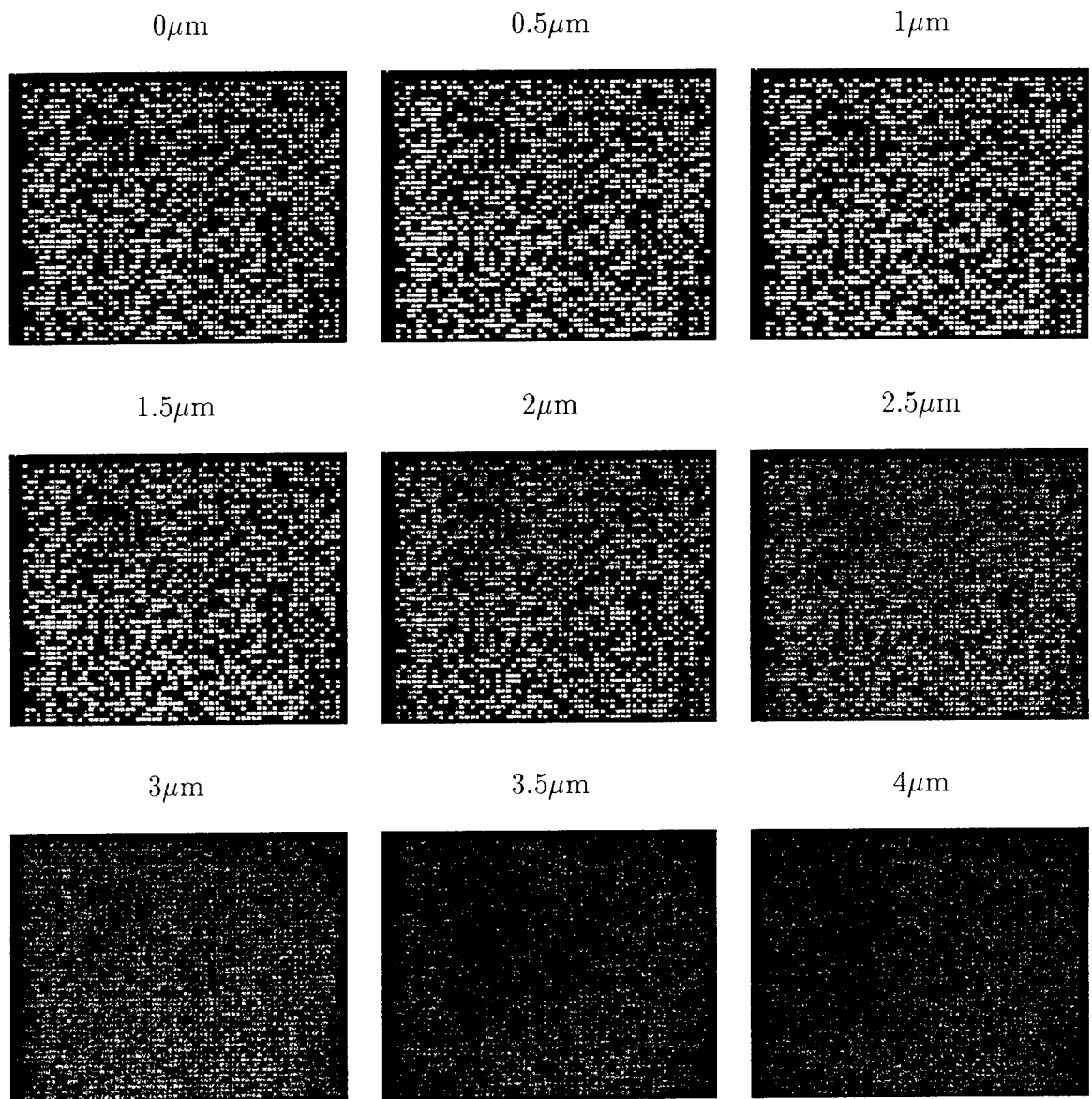


Figure 30: Bragg–mismatch of one of 10,000 holograms by translation of the focused spot on the mirror array.

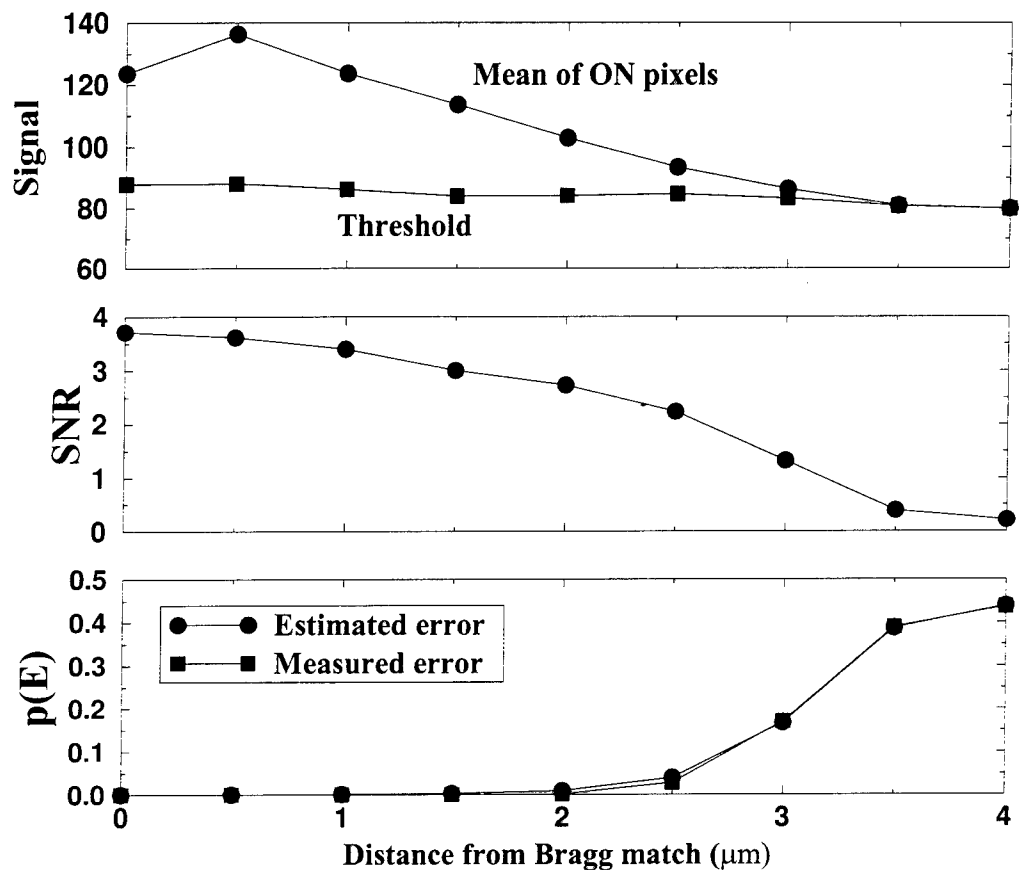


Figure 31: Analysis of images from Bragg-mismatching sequence shown in Figure 30. Plotted as a function of shift in focused spot (angle mismatch) are the mean of the ON pixel regions and value of the optimal threshold, the SNR, and measured and estimated probabilities of error.

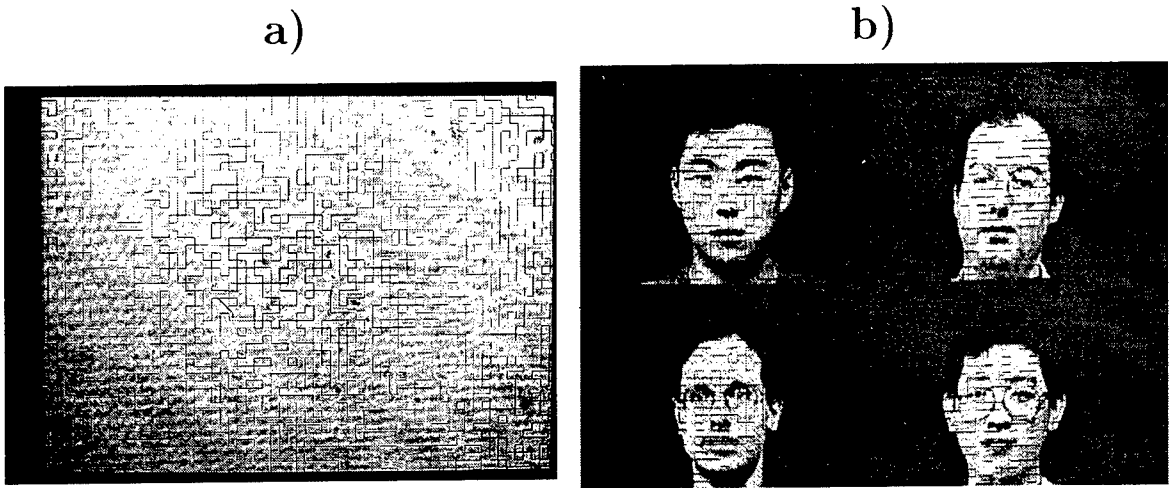


Figure 32: Images showing lines from random phase plate: a) image through crystal, b) one of 10,000 holograms at top location.

previous 10,000 hologram experiments had all been in the Fresnel plane because we did not have our own random phase plate to spread out the DC (zero spatial frequency) power of the object beam. So to demonstrate the 160,000 hologram system, we fabricated a random phase plate.

We will discuss the fabrication of the phase plate later. Here we discuss how we integrated the random phase plate into our system. We found that even transition widths of $6\mu\text{m}$ between the regions of 0 and π phase showed up as dark lines on the detected images. For example, in Figure 32, we show a blank screen imaged through the system, as well as one of the 10,000 holograms: a grey-scale image of faces. The random pattern of the phase plate is clearly visible. This particular phase plate contained one phase region for every 8×8 SLM pixels. We also tried 2×2 and 4×4 phase plates, but chose to use an 8×8 phase plate because the transition widths were the smallest, there was no speckle in the transmitted images, and we could hide the phase plate lines through careful choice of display patterns.

We were able to keep the lines of the random phase plate transitions from showing up in our reconstructions by turning off the pixels on the SLM in a series of cross-hatched lines which exactly overlapped the phase plate transitions. After this, we had a set of 60×50 pixel regions as shown in Figure 33. The phase plates were made with masks that were slightly too small—the most noticeable effect of this is that one of the rows near the center of the

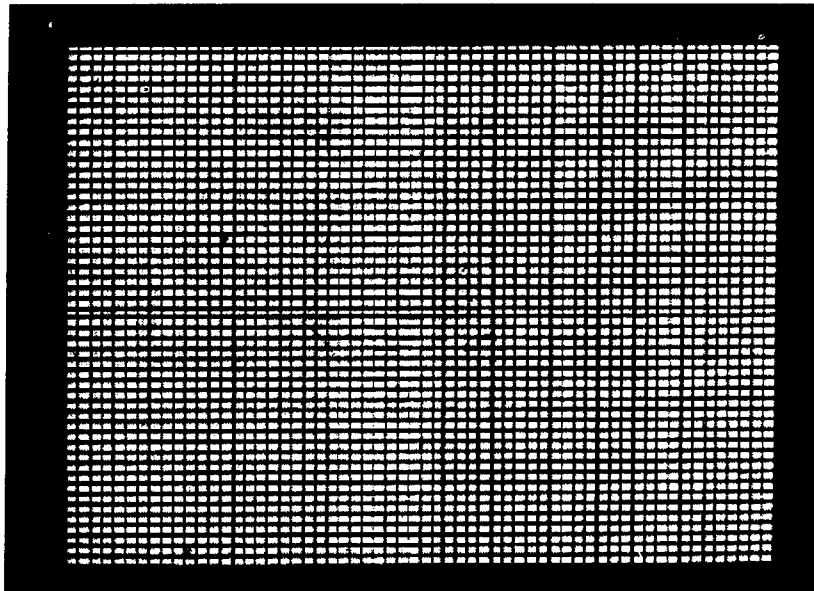


Figure 33: Set of 60×50 pixel regions used to avoid random phase plate lines.

pattern is thinner than the rest. The mismatch in the horizontal direction is not as noticeable since we had more flexible control over the columns than over the rows. We had 640 vertical columns to play with on the VGA screen, with only 200 rows. The pattern that we display on this VGA monitor gets mapped to a 480×400 windows on the 480×440 SLM and then imaged onto the center of the 60×55 phase plate.

We placed the random phase plate in the first image plane after the SLM, as shown in Figure 34. We put the object beam through a spatial filter and a polarizer before illuminating the random phase plate. If we had placed the polarizer after the phase plate, light would still strike the random phase plate transitions. Even though we had set those SLM pixels OFF, light was only modulated in polarization and would still illuminate the phase plate transitions. This light would have scattered throughout the object beam, causing distortions in the stored holograms. By placing the polarizer before the phase plate, we removed this fixed pattern noise light. The disadvantage to this was that we had to use a sheet polarizer, which was less efficient and introduced interference fringes in the object beam.

The random phase plate and the SLM were each mounted on rotational

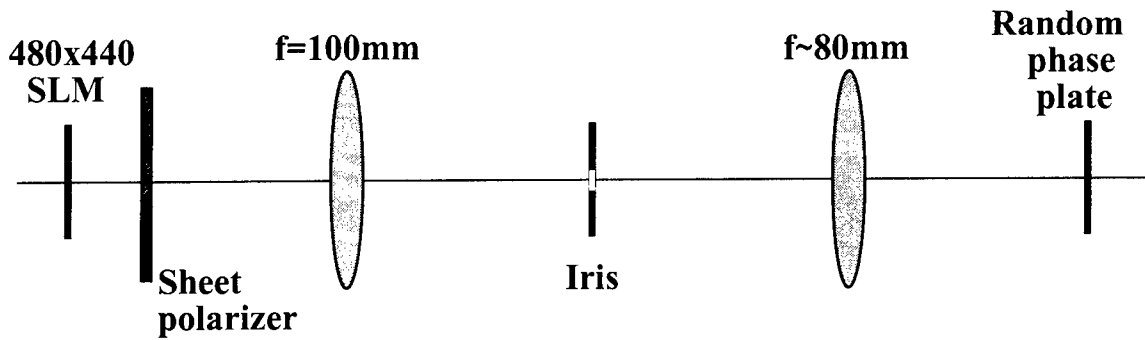


Figure 34: Object arm, shown between the SLM and the random phase plate.

stages which were then mounted on a 3-axis translation stages. The remainder of the object beam was as shown in Figure 27, where the plane marked as “Input SLM” corresponds to the plane where the demagnified SLM image overlapped the random phase plate. The lens f_{object} was of focal length 200mm and aperture 70mm, as was the lens immediately after the crystal. The reconstructed images were imaged and further demagnified onto the detector array with a 4-F system composed of an $f = 80\text{mm}$, 50mm aperture achromat and a f/1.6 camera lens “focused” on infinity (effective back focal length: 50mm). The camera was a STAR I cooled CCD camera, with 576×384 detector pixels. Each pixel was $23\mu\text{m}$ square, with unity fill factor. The reconstructed holograms we show below are 540×360 detector pixels in size, which includes a small border around the holographic data.

Description of the experiment —We stored 30,000 holograms in a LiNbO₃:Fe crystal of dimensions $1.5\text{cm} \times 2\text{cm} \times 4\text{cm}$. We used locations #1, #9, and #16, corresponding to the bottom, center, and top locations of our 160,000 hologram system. The crystal was fabricated from a 0.015% Fe-doped LiNbO₃ boule donated by Crystal Technologies, and was not anti-reflection coated. Because a 2 inch half-waveplate was not available, we used a 1 inch half-waveplate and translated it vertically to access the different locations. The edges of the crystal were masked off with electrical tape, and the entire object beam after the crystal sealed from all light save the exit aperture of the crystal. An iris was mounted on a two-axis translation stage for movement in the plane marked “IRIS Plane” in Figure 27. This was translated to the appropriate height for reconstruction of holograms from a

particular location. The camera received a larger amount of scattered light if this iris was not in place. Although the holograms were still easily observable, we closed down the iris to cut down on the scattered light. Although a moving iris is not a practical solution in a fast memory, a fixed array of slits, aligned with the Fourier transforms of the various locations, might be a reasonable compromise for a practical system.

Each set of 10,000 holograms was stored with 4 fractal rows of 2500 holograms each. Within each fractal row, all holograms were spaced by $10\mu\text{m}$. For most fractal rows, the translation of the focused spot spanned a horizontal translation range of -12.5mm to +12.5mm, where 0mm corresponds to the horizontal optical axis of the Fresnel lens. A few mirror strips, however, were used from -15mm to +10mm to avoid damaged spots on the mirror strips. The limit on the angle multiplexing range in our experiment was the aperture of the 1 inch waveplate (which was placed 2mm from the crystal surface). With a 2in waveplate, we could have used an angle range from -25mm to +25mm. Since the angle spacing between holograms was comfortably large, we had more than enough reference beams for 20,000 or even 25,000 holograms per location.

Dynamic range, however, was a different matter. We reduced the background scattering by eliminating all stray light from the object beam path for reconstruction. In order to use all of the horizontal extent of the crystal within each vertical location, we deflected the object beam horizontally to spread the 10,000 holograms throughout the crystal. We had hoped that this deflection would avoid any distortion caused by overexposure at the focused DC spot of the image. Without the random phase plate, however, we observed an unacceptable amount of distortion and stray light in the regions of OFF pixels. With the random phase plate, even though it only contained one phase pixel per every 8 SLM pixels, the power in the DC was dispersed enough that the distortion disappeared. We deflected the signal horizontally across the width of the crystal, completing 50 complete cycles during the storage of 10,000 holograms. Since the reference beam was slightly larger than the size of the focused spot, we deflected the object beam vertically within the storage location by a small random amount along with each horizontal movement. This vertical deflection of the object beam was constrained to be within reasonably tight limits, so that the object and reference achieved good overlap for all holograms.

We observed no strong trend in diffraction efficiency between holograms written with object beams close to the reference beam and those written on

the far side of the crystal. This would be expected for most of the holograms in the schedule, since holograms remote from the entrance face of the reference beam would have poorer modulation depth yet slower erasure from the reference beam. We would expect that only the holograms written in the last pass of the signal beam through the crystal would be unequal in diffraction efficiency, since for these holograms, little or no erasure occurred between recording and readout. This nonuniformity can be easily counteracted by minor adjustment of the recording times for these last few holograms.

Analysis of the reconstructions We captured reconstructions from the center, top, and bottom locations, using a 1 second exposure with the STAR camera. These included several chessboard images, the Caltech logo, and a mosaic of faces. Most reconstructions, however, were random data pages based on the 60×50 grid described above. Of these images, there were 23 reconstructions from the center location, 22 from the bottom, and 28 from the top. Many of these reconstructions are shown in Figure 35, 36, and 37. One original image—a random page imaged through the crystal—is shown in Figure 22 for comparison. The characteristics of these data images are plotted in Figure 38, including the means of the ON and OFF pixel regions, the optimal threshold, the SNR, and estimated probability of error of the reconstructed holograms. The holograms chosen for analysis were well distributed among the 30,000 holograms.

In the experiments we described previously, we analyzed SNR by treating each detector pixel within a region as a separate sample. By using large regions of ON and OFF pixels and throwing out edge pixels, we simplified the assignment of locations and were assured that the SLM did not introduce electrical crosstalk noise. With the lines introduced by the phase plate, however, we could no longer use large regions. For this experiment, therefore, we decided to average all of the detector pixels within each pixel region to create sample points for analysis. This gives us, on average, 1500 ON pixel regions and 1500 OFF regions. The effects of SLM nonuniformity across a pixel region get averaged out. However, we still needed to assign the ON and OFF regions—to draw a box around each region. We cannot use boxes which fill the detector area, though, because the ON regions are smaller than the spacing (the fill factor is less than 1). A further complication is a variance in the size of the pixel regions—caused by the mismatch between the phase plate and the SLM image. Finally, a slight rotation and bending of the

Center location

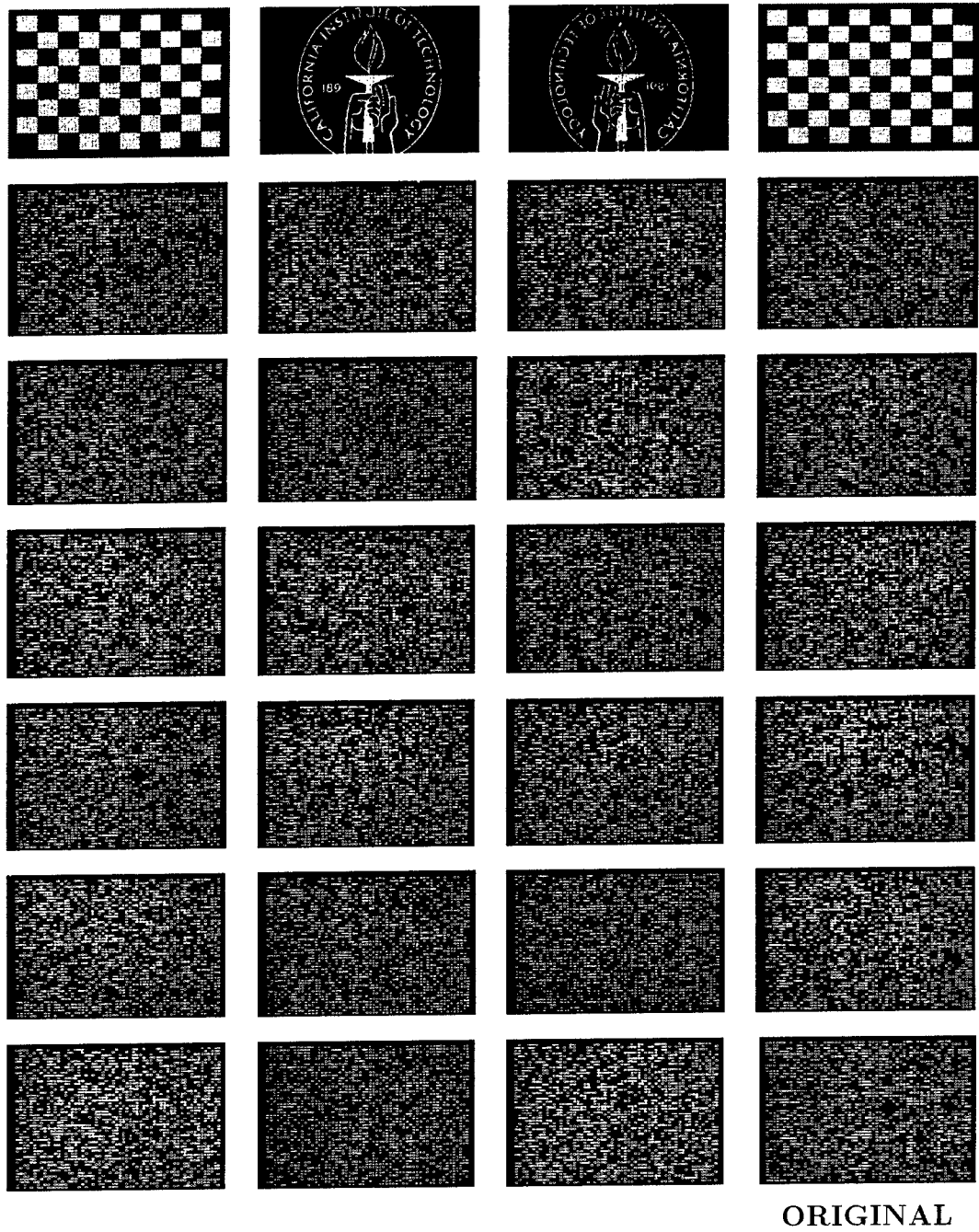


Figure 35: Storage of 10,000 holograms at center location (#9)

Bottom location

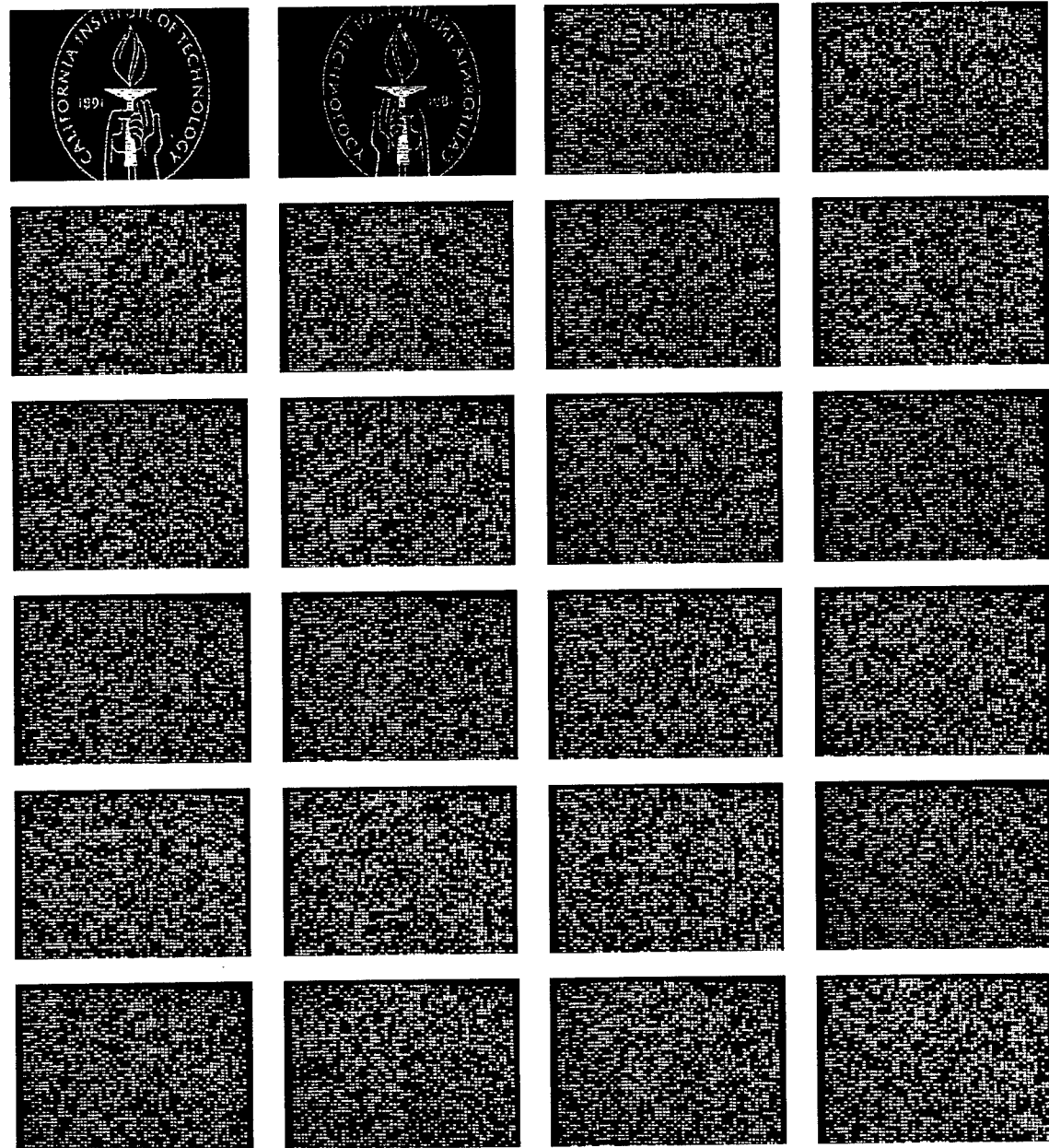


Figure 36: Storage of 10,000 holograms at bottom location (#1)

Top location

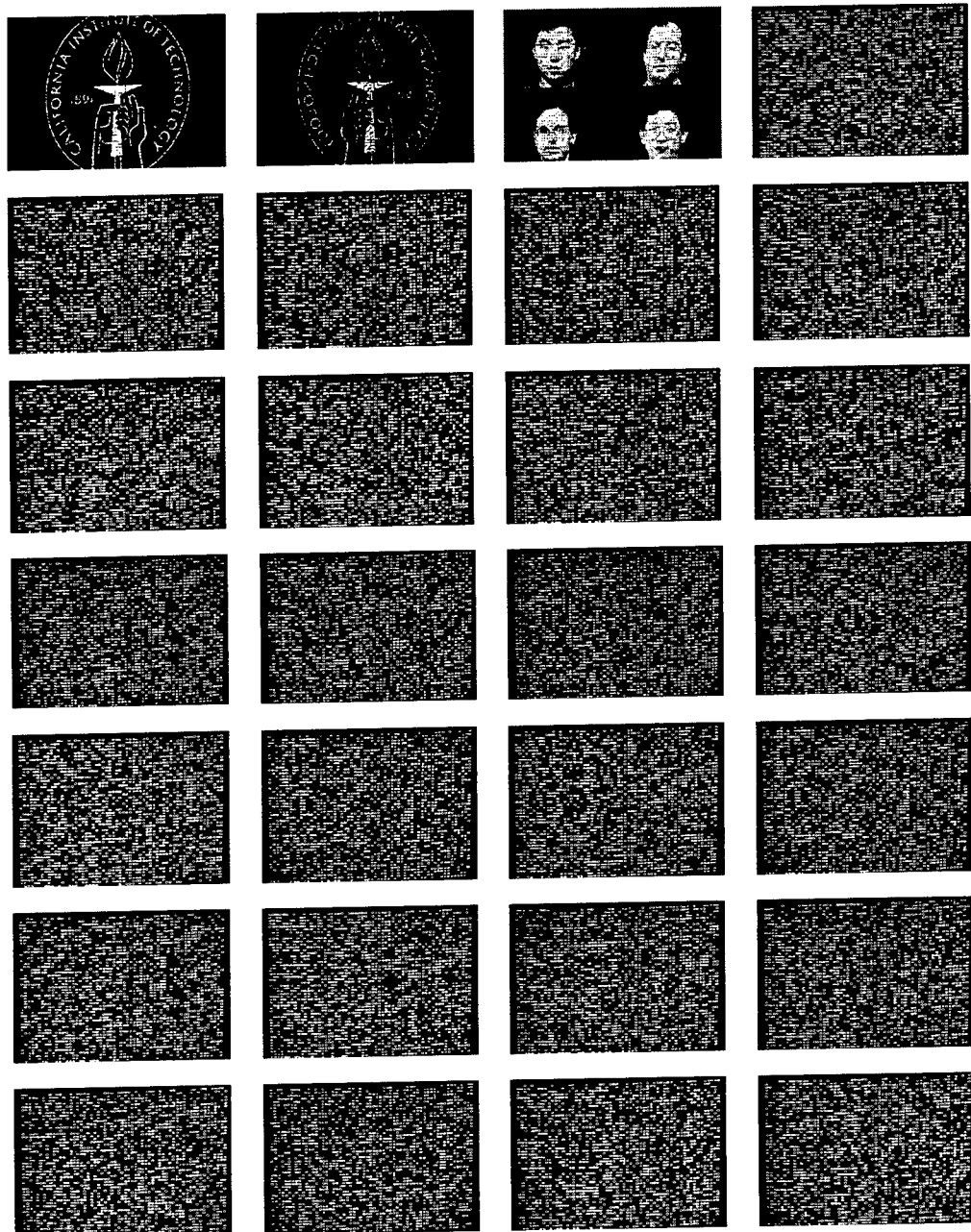


Figure 37: Storage of 10,000 holograms at top location (#16)

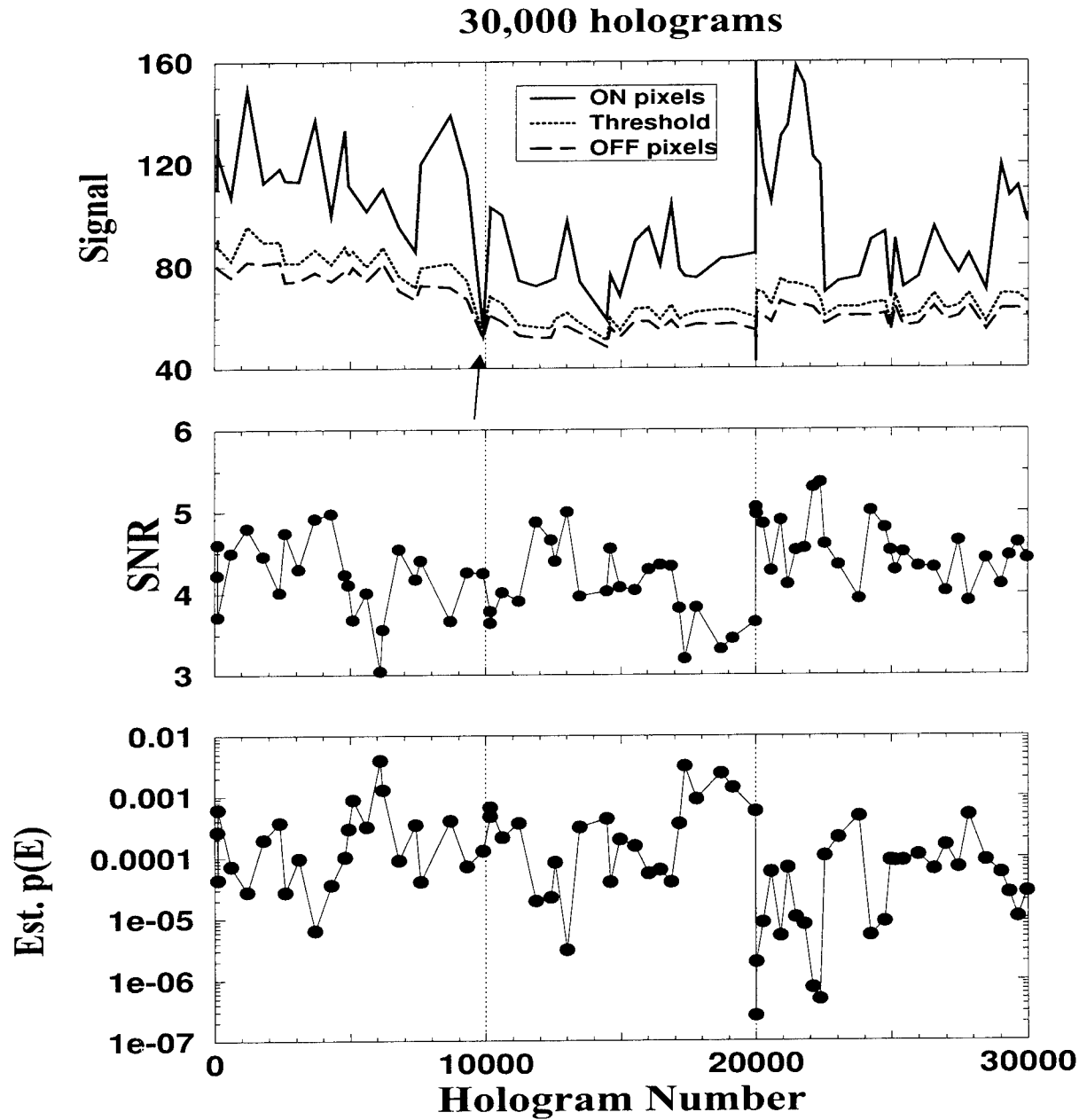


Figure 38: Analysis of data-bearing images from Figures 35–37. Plotted as a function of hologram number are the means of the ON and OFF pixel regions, value of the optimal threshold, SNR, and both measured and estimated probability of error.

images occurred at the extreme locations. It is not immediately observable in the images we show in Figures 36, but you can see it if you look for it. We might hope to use a “grid” of pixel regions which is aligned with the rows and columns of detector pixels. However, even a mild rotation of the SLM image causes this grid to fail to register with the pixel regions. In practice, the rotation could be avoided by a routine for rapid SNR analysis in the laboratory, perhaps configured to automatically translate and rotate the SLM and detector until they are registered to each other.

Despite the slight distortions of our images, we wanted a quantitative measure of our holograms. However, given a reconstructed image from a particular location, each of the 3000 possible ON pixel regions shows up at some unknown box of detector pixels. The relative spacing between each box, and the relative width of the boxes does not change. For example, we might know that column #25 always has narrower boxes than the other columns, or that the spacing between row #16 and its neighbors is always a bit more than between the other rows. The only thing which changed was where these columns and rows of boxes appear, and whether they might be bent a little. We devised a computer analysis method in which we manually aligned a grid pattern from one of the reconstructed images, and then used it to analyze all the other reconstructions from the same location. We first manually aligned 42 boxes in a sparse pattern as shown in Figure 39 , matching these against one of the captured reconstructions. In terms of the grid of 3000 boxes, these boxes corresponded to the intersections of the 1st, 10th, 20th, 30th, 40th, 50th, and 60th columns with the 1st, 10th, 20th, 30th, 40th, and 50th rows. After these were set, we interpolated the full pattern of 3000 boxes using our knowledge of the relative spacing and widths of the various rows and columns. The center of each box was determined by interpolation; the width and height set to 70% of the distance to the nearest neighbor box. Each box coordinate is then rounded to the nearest integer. At this point, we have a grid of 3000 boxes—an example of one grid from the top location is shown in Figure 40.

The next step was to divide this appropriately into the classes of ON and OFF pixels. We did not want to choose the ON and OFF pixels from the reconstructions, since we wanted to know that we were comparing the results against what had been stored. Instead, before the experiment began, we created 100 random patterns to be displayed on the SLM and saved the 3000 bit sequence associated with each. Then, when we went to analyze each reconstruction, we first determined which of the 100 pages were represented

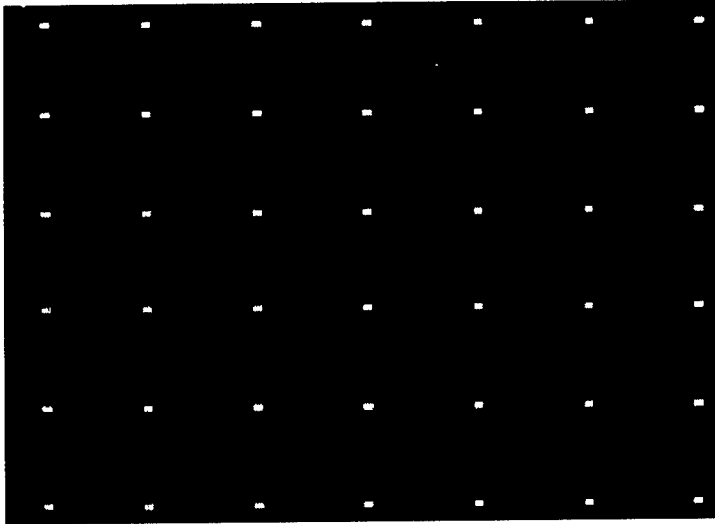


Figure 39: Sparse grid of 42 pixel regions aligned manually and then used for interpolation.

by visual inspection and comparison with our small database of bit sequences. This gave us the correct assignment of the grid of 3000 boxes into the classes of ON and OFF regions.

We found that the reconstructions tended to be shifted by a few detector pixels from each other because they were stored at different locations in the crystal. As we mentioned above, the deflecting mirrors were not in exactly the image plane, so we got small movements of the image plane along with larger movements of the focused image beam in the Fourier plane. For each reconstruction, we shifted the entire grid by a few detector pixels in either direction to find the maximum SNR. We tried to use the same set of 3000 boxes for all of the reconstructions from a particular location, keeping the interbox spacings identical. For instance, all of the reconstructions in Figure 36 were analyzed with one grid pattern. For the other locations, we occasionally needed to realign the sparse grid of 42 boxes and then reinterpolate. If we did not realign the grid, the SNR would tend to drop to between 2.5 and 3. We do not believe that this change in interbox spacing was due to changes in the aberrations encountered, since reconstructions from the center location needed realignment as often as those from the top location. Instead,

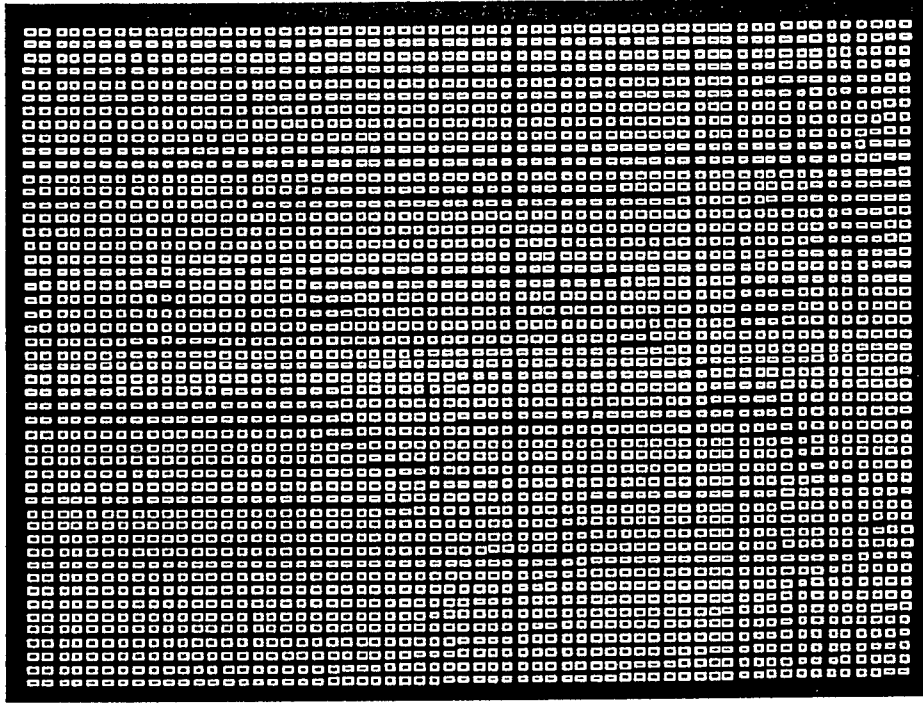


Figure 40: Grid of 3000 pixel regions formed by interpolating the sparse grid pattern.

the change in the grid patterns probably stemmed from the slightly varying optical path lengths encountered as the signal beam was moved back and forth within the storage location. This occurred even though the crystal was professionally polished. The solution to this problem is phase-conjugate readout, which is one of the directions of our future work.

Note that one of the reconstructions in Figure 38 (marked with an arrow) appears to be much weaker than the others. This particular reconstruction was captured with a 0.2 second exposure. It is important to note that the SNR and probability of error are unaffected by the shorter exposure time. This means that we could have used this shorter exposure for all of the holograms. The reason we did not is that we wanted enough dynamic range in the reconstructions to be able to display the images in PostScript greyscale. In terms of a practical system, the application of the threshold should take place in analog at or close to the pixel. This reduces the I/O output of the pixel to exactly the number of information bits and reduces the quantization error of the thresholding operation to the resolution of the analog comparator.

3.5 Miscellaneous experiments

Simultaneous memory and correlator One of the other applications that we demonstrated with our memory setup was the implementation of real-time face recognition, where stored holograms are used as correlation templates. Holograms are read out with the signal beam, reconstructing the appropriate reference beams. The strength of each reference beam is proportional to the correlation between the image used originally for storage, and the image being displayed in real-time on the SLM. The reference beams can be focused onto a detector, forming correlation peaks. Because the holograms have Bragg-degeneracy in the vertical direction, the system has vertical shift invariance. In other words, the input face can be shifted vertically and the correlation peak shifts along with it. If the input face is shifted horizontally, then the correlation peak disappears through Bragg mismatch.

We used a setup similar to the 160,000 hologram setup for this experiment. As shown in Figure 41, we used the mirror array to direct the reference beams and our standard object beam for deflecting the SLM signal. We mounted the SLM sideways so most of the natural side-to-side face motion would be vertical motion in the system, for which we had shift invariance. Our first experiment was the demonstration of memory storage in one location and face-recognition at a neighboring location. First, we stored holograms in the upper portion of our crystal.⁶ The Fourier transform plane of the object beam was in front of the crystal. After these holograms were stored, we changed the incoming portion of the object beam of the system to prepare for correlation.

In the object beam, we placed a DC block in the Fourier transform plane of the SLM. This spatially filters the images presented to the crystal, both during storage and during real-time correlation. Without a DC block, it is difficult for the system to distinguish one image from another, because each image contains so much DC energy. Although the edge-enhanced images contain much less energy, the discrimination performance is significantly improved. We placed a rectangular aperture in a subsequent image plane to block the edge-enhanced borders of the picture and further improve the discrimination performance. Finally, we replaced lens L_3 with a shorter focal length lens. Although this makes it impossible to have the SLM image plane coincide with the back focal plane of lens L_3 , we can place the Fourier trans-

⁶The crystal was a 23mm × 23mm × 13mm 90° geometry crystal cut from a 0.015% Fe-doped LiNbO₃ boule donated by Crystal Technologies.

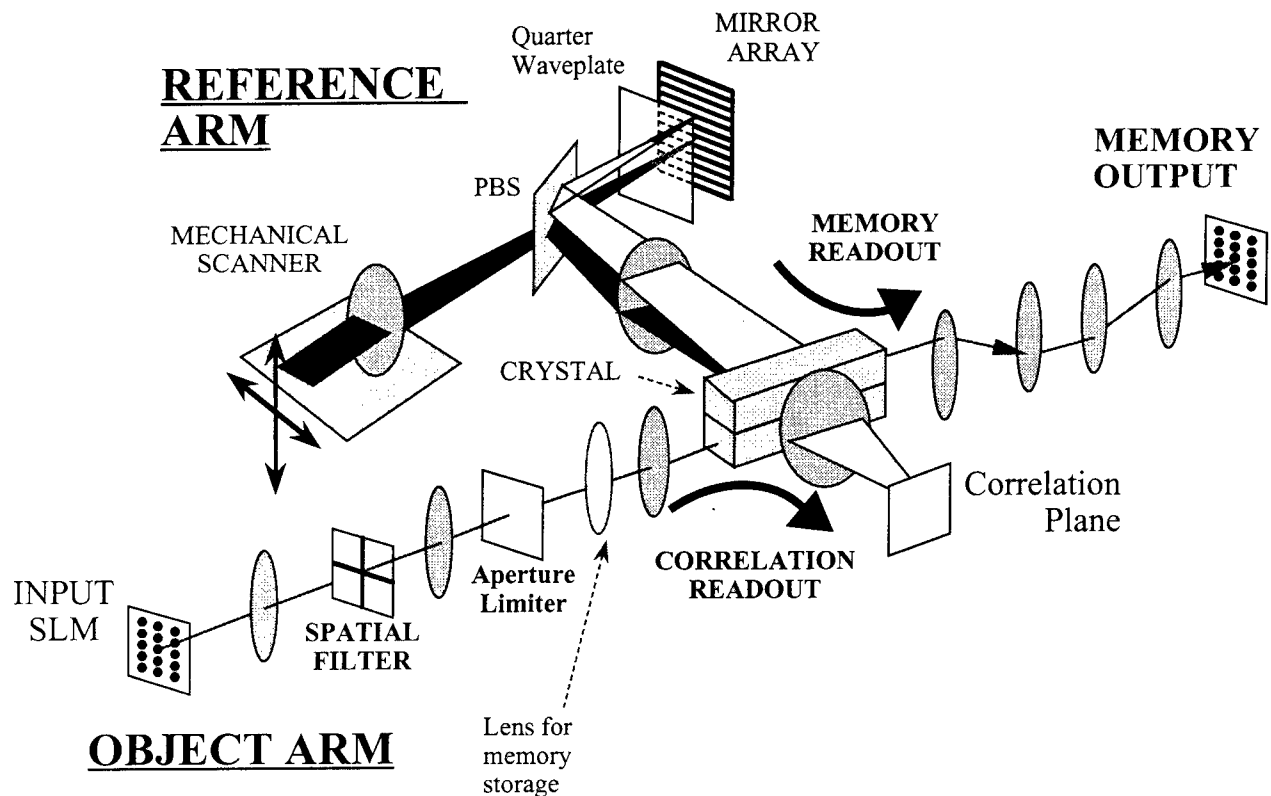


Figure 41: Simultaneous memory and correlator: experimental setup

form of the edge-enhanced image directly within the crystal. If the crystal is not exactly at this Fourier transform plane, then the shift invariance is reduced. There was not much that we needed to do in the reference arm, because the mirror array allows us to store at a different location simply by translating the mechanical scanner.

We used several fractal rows to store correlation templates. In this first demonstration, we had a correlation database of 60 separate images each of 4 people. We used one fractal row for each person. To read out the correlation peaks, we placed a f/1.6 camera lens at the side face of the crystal as shown in Figure 41 and a CCD detector at its focal plane. Note that the correlation plane is the image of the mirror array surface—therefore we expect that the different fractal rows will be separated by some distance (corresponding to the mirror strips for the 15 other locations). We show this in Figure 42, where there are 6 “lines” or fractal rows of correlation peaks. We’ll keep referring to these as fractal rows even though they appear as columns in these pictures. We were able to readout the memory and the correlation peaks at the same time by using the mirror array to deflect the reference beam back to the top location. In Figure 43, we show several examples of the output of the two CCD detectors: one portion of the picture shows the correlation plane, while the other shows the reconstructed memory. Note that since the correlation templates were taken from a sequential video sequence, an input face often correlates with several similar templates.

Having demonstrated memory and correlation, we concentrating on increasing the number of stored templates. We were not really limited by any geometric limits, despite the fact that the correlation plane detector does not cover the full image of the mirror array. The reason is that we have no need to distinguish individual correlation peaks within the same fractal row. We can then place them closer together than the angular selectivity. The limit to the number of templates is mostly dynamic range. We have an advantage here over memory readout, because the reconstructed wavefront is detected at its high-intensity focus. However, we’re also at a disadvantage because the edge-enhanced input image input to the crystal contains very little power, on the order of $1\text{-}10\mu\text{W}$.

We used the nonlinear filtering capabilities of the Imagepoint camera to enhance the correlation peaks, which essentially picks a threshold below which we cannot distinguish the peak. We were able to store 1200 correlation templates, arranged in 6 fractal rows of 200 templates each. As above, each fractal row corresponded to templates from a single individual. We show

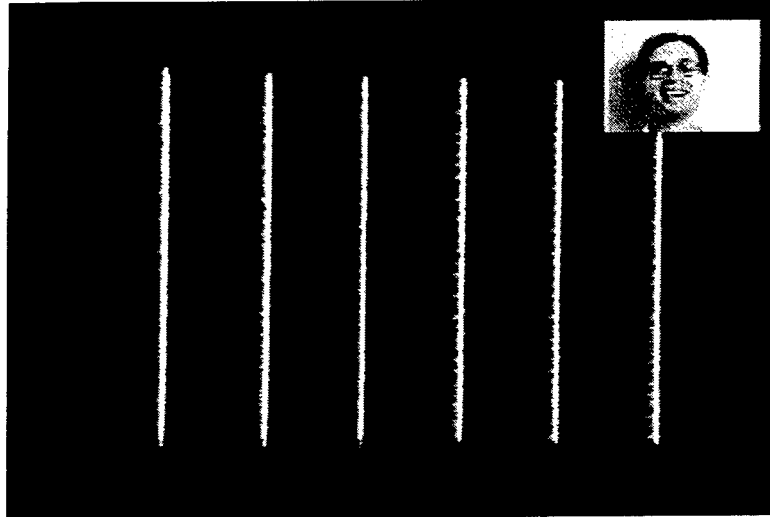


Figure 42: The correlation plane

several examples of real-time correlation in Figure 44. In these images, the corner image is the input image and the remainder of the frame is the correlation plane.

Thermal fixing of multiple holograms We used the 160,000 hologram setup to demonstrate fixing. In order to be able to find the holograms after replacement of the crystal, we used a glass plano-convex lens of 70mm focal length, 60mm aperture in the reference arm. We recorded 1000 holograms at the same $10\mu\text{m}$ reference beam spacing. After recording the holograms, we observed a few reconstructions. We removed the crystal from the apparatus and immediately replaced to observe the degradations caused by imperfect crystal positioning. We observed that, even with the glass lens, the uniformity of the holograms was seriously affected by the simple act of removing and replacing the crystal. This is probably an effect of the poor plane wave quality of the reference beam after 4 cylindrical lenses and could be corrected by the use of diffractive optics for beam shaping.

After removing the crystal again, we placed it in an oven for 30 minutes. The oven had been preheated to 120° C . After cooling, the crystal was replaced in the setup and illuminated. As expected, no holograms were immediately observed as the ionic gratings compensated the charge gratings. Two experiments were performed: in the first, we illuminated the crystal

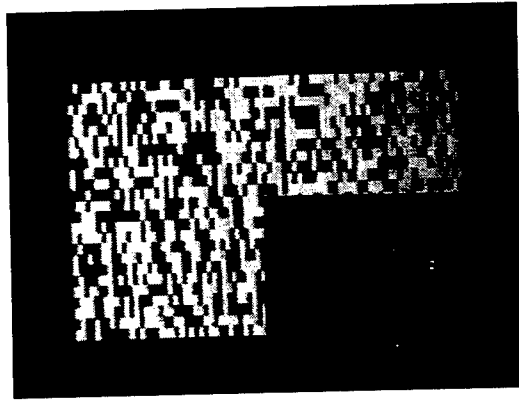


Figure 43: Simultaneous memory readout and real-time correlation.

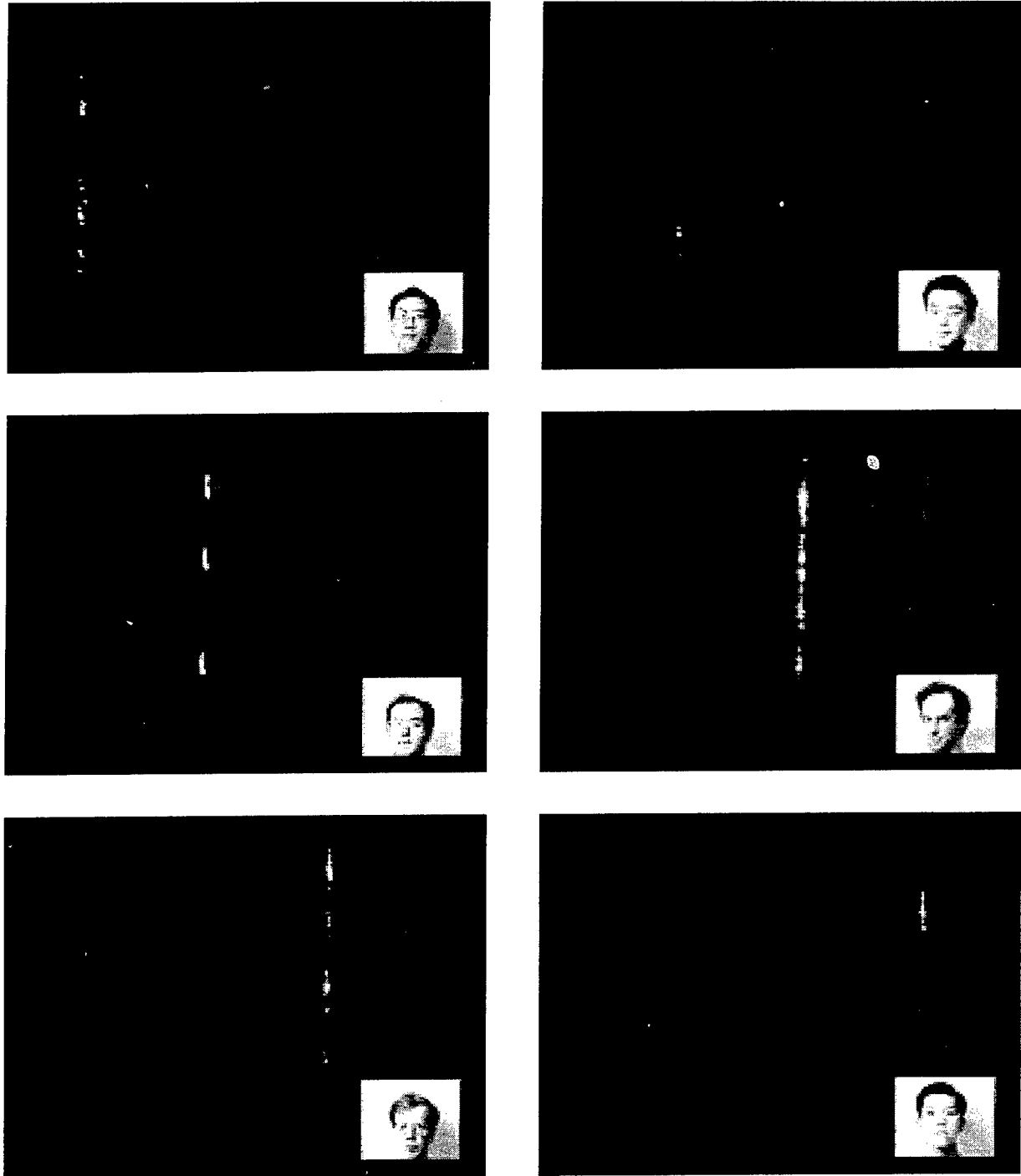


Figure 44: Demonstration of a real-time face correlator with 1200 face images

(erasing the charge gratings) with UV illumination for 210 minutes. We observed that approximately 27% of the original diffraction efficiency was retained by the fixed holograms. The observed degradations of the images did not differ much from those seen after the first (non-fixed) replacement of the crystal. In the second experiment of 1000 holograms, we illuminated the crystal with the 30mW reference beam. The reference beam was swept through the full range continuously in order to avoid any fanning buildup which might occur. After 210 minutes, approximately 30% of the original diffraction efficiency was retained by the fixed holograms. Figure 45 shows reconstructions of fixed holograms from both of these experiments. The top 6 images correspond to the UV erasure experiment, and the bottom 6 to the reference beam erasure experiment.

No study of the SNR is shown because we found that it depended too strongly on the accuracy of the repositioning. When we found holograms which were unsatisfactory in fidelity, we could reposition the crystal and improve the uniformity and diffraction efficiency substantially. However, we have no way of knowing if the exact same holograms were improving, or whether we were looking at different holograms each time. In order to study the SNR of fixed holograms carefully, one must find a way to either fix in situ, or to reposition the crystal with very high accuracy.

Random-phase plate This is the procedure we used to fabricate the random phase plates. Xin An and Geoff Burr made the masks used for lithography, including the determination of the required size. Annette Grot developed and performed the processing procedure.

The procedure has essentially three parts: Put a layer of photoresist onto a clean glass substrate, expose portions of the photoresist through a contact mask, and then etch the glass in these regions with acid. The substrate can be cleaned with soap and water and then chromic sulfuric acid, rinsed, blown dry with N₂, and dried on a hot plate. Photoresist primer is spun on the substrate at 2000 rpm for 10 sec, followed by photoresist at 4500 rpm for 40 seconds. The photoresist is baked on a hot plate at 90°C for 90 seconds to remove some of the solvents.

At this point, the photoresist is ready to be exposed. We determined the size of the mask to use by placing a photoresist-coated glass plate in our optical system in the plane where the random phase plate was to go (Figure 34). The pattern of the fully illuminated SLM was then imprinted into the

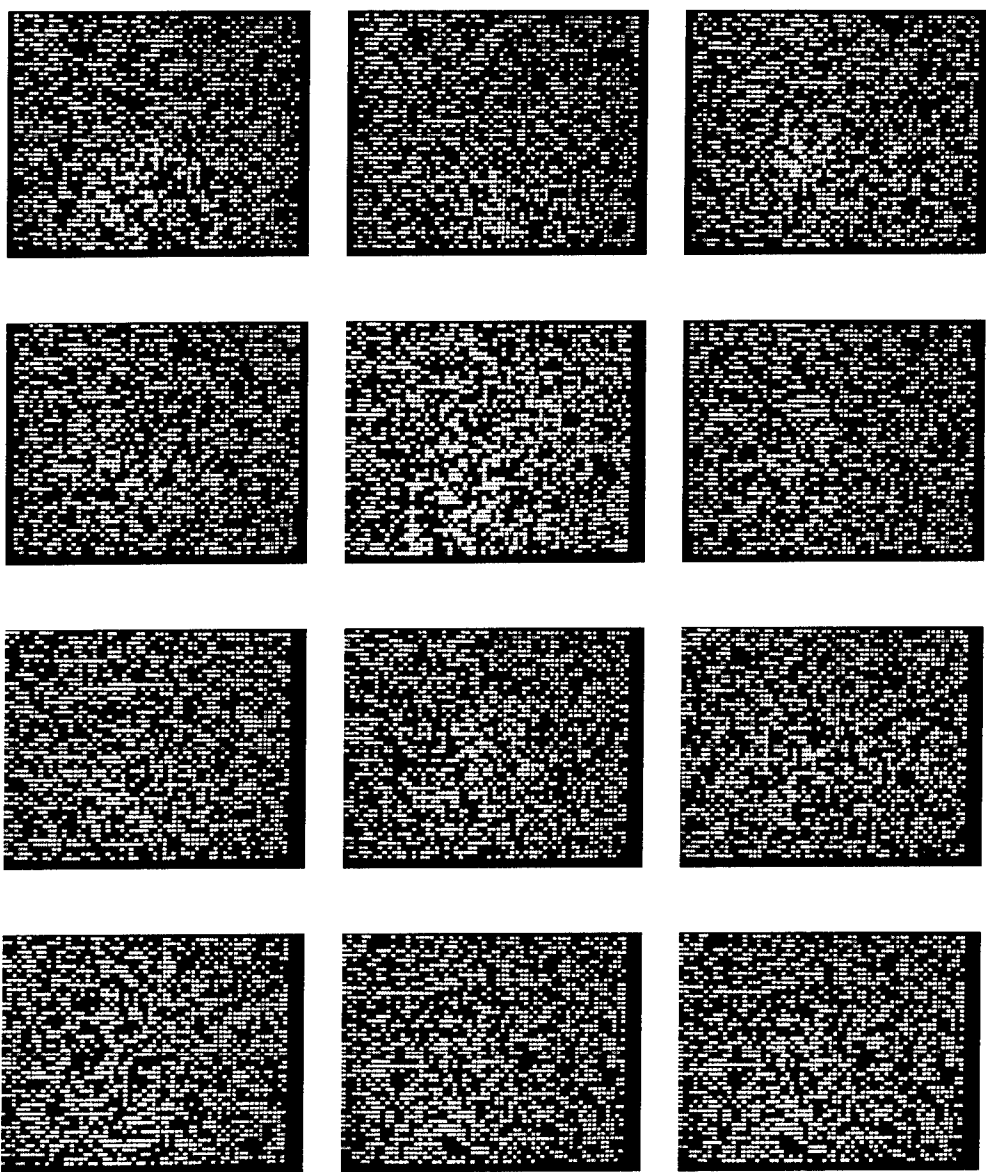


Figure 45: Storage of 1,000 fixed holograms. Shown are reconstructions from two separate experiments.

photoresist. After developing the photoresist, we used a Sloan Dektak II surface profilometer to determine the required spacing to within 1 part in 100. The resulting vertical spacing was $29.4\mu\text{m}$; the horizontal spacing was $35.7\mu\text{m}$. However, we needed to have these numbers accurate to better than 1 part in 500. To further zero in on the precise values, we had a mask commercially⁷ printed on transparent film with a 3386 dot-per-inch printer. We then checked the alignment of the exposed photoresist (representing the image of the SLM) against the mask. This led to another cycle of mask-printing.

Once we got close to the desired mask, we etched the patterns into the glass plates as follows. A contact mask aligner (Karl Suss MJB3) was used to expose a photoresist-coated glass plate. The plate was developed for 2 minutes and then baked on the hot plate for 2 minutes. The quality of the photoresist pattern was checked under a microscope before etching. The baking of the photoresist retards undercutting of the acid from regions of low phase (where we want the glass to be etched) into regions of high phase (where we want the glass to be protected by photoresist). This undercutting was the primary source of soft transitions between the two phase levels. The etchant we used was 1:10 hydrofluoric acid: water, and the substrate was immersed for approximately 50 seconds to reach the target etch depth of 5000\AA .⁸

The best transition width that we were able to fabricate was $6\mu\text{m}$, as shown in a Dektak trace in Figure 46. Note that a slight underetching of the entire pattern helped keep the transition width low—conversely, for slight overetching, the transition width became much larger. The transition shown in Figure 46 was measured on the 8×8 phase plate we used in our 30,000 hologram experiment. The 8×8 refers to the number of SLM pixels within each phase region. We fabricated several 4×4 and 2×2 phase plates, with transition widths ranging from $7\text{--}13\mu\text{m}$.

When we placed the phase plates in the optical system, aligned them to the SLM image and observed the resulting image with the detector array, we found that we were unable to make the transition lines entirely disappear. We had originally expected that, if these lines were appearing to mismatch in the size of the mask, we would be able to translate the phase mask and observe movement in the visible phase plate lines. This would take place as some

⁷The cost per page was <\$25.

⁸We wanted $(n - 1)d$ to be approximately $\lambda/2$, where λ was 488nm and $n \sim 1.5$.

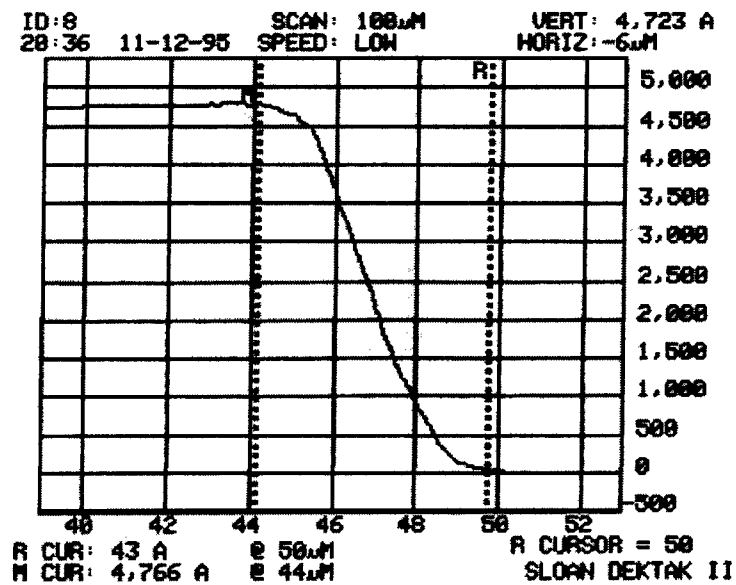


Figure 46: Surface profile of transition from π to 0 phase.

phase plate transitions moved into the gaps between SLM pixels while others moved out of these gaps. Instead, what we observed was that the visibility of the phase plate lines depended mostly on radial distance from the center of the SLM. If the lines in the center disappeared, those at the edge were quite visible. We also found that we could reverse this situation by refocusing the phase plate, making the transition lines in the center noticeable and those at the edge invisible. In practice, we focused the phase plate to where the phase plate transitions were moderately visible in both the center and at the edges, and invisible in a ring about the center. This is the condition that is shown in Figure 32(a).

When we went through the process of determining which pixels on the display needed to be turned off in order to hide the phase plate transitions, we discovered that the phase plate was approximately 2 SLM pixels too small. By the time we got another mask made in preparation for making new phase plates, our experiments with the first were progressing so well that we were reluctant to make a change.

MISSION OF ROME LABORATORY

Mission. The mission of Rome Laboratory is to advance the science and technologies of command, control, communications and intelligence and to transition them into systems to meet customer needs. To achieve this, Rome Lab:

- a. Conducts vigorous research, development and test programs in all applicable technologies;
- b. Transitions technology to current and future systems to improve operational capability, readiness, and supportability;
- c. Provides a full range of technical support to Air Force Material Command product centers and other Air Force organizations;
- d. Promotes transfer of technology to the private sector;
- e. Maintains leading edge technological expertise in the areas of surveillance, communications, command and control, intelligence, reliability science, electro-magnetic technology, photonics, signal processing, and computational science.

The thrust areas of technical competence include: Surveillance, Communications, Command and Control, Intelligence, Signal Processing, Computer Science and Technology, Electromagnetic Technology, Photonics and Reliability Sciences.